Supermassive black hole winds in X-rays: SUBWAYS: I. Ultra-fast outflows in quasars beyond the local universe

Matzeu, G.A.; Brusa, M.; Lanzuisi, G.; Dadina, M.; Bianchi, S.; Kriss, G.; ... ; Merloni, A.

Supermassive Black Hole Winds in X-rays: SUBWAYS

I. Ultra-fast outflows in quasars beyond the local Universe

G. A. Matzeu[1,2,3], M. Brusa[1,2], G. Lanzuisi[2], M. Dadina[2], S. Bianchi[4], G. Kriss[5], M. Mehdipour[5], E. Nardini[6],
G. Chartas[7], R. Middei[8], E. Piconcelli[9], V. Gianolli[4,10], A. Comastri[2], A. L. Longinotti[11], Y. Krongold[11], F. Ricci[4],
P. O. Petrucci[10], F. Tombesi[12,9,13,14], A. Luminari[15,9], L. Zappacosta[9], G. Miniutti[16], M. Gaspari[17], E. Behar[18],
M. Bischetti[19], S. Mathur[20,21], M. Perna[16], M. Giustini[16], P. Grandi[2], E. Torresi[2], C. Vignali[1,2], G. Bruni[15],
M. Cappi[2], E. Costantini[22], G. Cresci[6], B. De Marco[23], A. De Rosa[15], R. Gilli[2], M. Guainazzi[24], J. Kaastra[22,25],
S. Kraemer[26], F. La Franca[4], A. Marconi[27], F. Panessa[15], G. Ponti[28], D. Proga[29], F. Ursini[4], P. Baldini[1], F. Fiore[19],
A. R. King[30], R. Maiolino[31,32], G. Matt[4], and A. Merloni[33]

(Affiliations can be found after the references)

ABSTRACT

We present a new X-ray spectroscopic study of 22 luminous ($2 \times 10^{45} \lesssim L_{\rm bol}/{\rm erg\,s^{-1}} \lesssim 2 \times 10^{46}$) active galactic nuclei (AGNs) at intermediate redshifts ($0.1 \lesssim z \lesssim 0.4$), as part of the SUpermassive Black hole Winds in the x-rAYS (SUBWAYS) sample, mostly composed of quasars and type 1 AGNs. Here, 17 targets were observed with *XMM-Newton* in 2019–2020, and the remaining 5 are from previous observations. The aim of this large campaign (1.45 Ms duration) is to characterise the various manifestations of winds in the X-rays driven from supermassive black holes in AGNs. In this paper we focus on the search for and characterisation of ultra-fast outflows (UFOs), which are typically detected through blueshifted absorption troughs in the Fe K band ($E > 7$ keV). By following Monte Carlo procedures, we confirm the detection of absorption lines corresponding to highly ionised iron (e.g. Fe XXV Hα and Fe XXVI Lyα) in 7 out of 22 sources at the ≳95% confidence level (for each individual line). The global combined probability of such absorption features in the sample is >99.9%. The SUBWAYS campaign, based on *XMM-Newton*, extends to higher luminosities and redshifts than previous local studies on Seyferts. We find a UFO detection fraction of ∼30% of the total sample, which is in agreement with previous findings. This work independently provides further support for the existence of highly ionised matter propagating at mildly relativistic speeds ($\gtrsim 0.1c$) in a considerable fraction of AGNs over a broad range of luminosities, which is believed to play a key role in the self-regulated AGN feeding-feedback cycle, as also supported by hydrodynamical multi-phase simulations.

Key words. galaxies: active – quasars: absorption lines – X-rays: galaxies – quasars: emission lines

1. Introduction

It is widely accepted that supermassive black holes (SMBHs; 10^6–10^{10} $M_\odot$; e.g. Salpeter 1964; Magorrian et al. 1998) are hosted at the centre of virtually every known massive galaxy. The observed tight correlations between the host galaxy and the SMBH properties (see Kormendy & Ho 2013, for a review) strongly suggest that their formation and evolution are profoundly coupled with each other. Some physical mechanisms must have therefore linked the regions where the SMBH gravitational field dominates to the larger scales, where its direct influence is negligible. At this stage, the key underlying ingredients at play in the co-evolution paradigms of active galactic nuclei (AGNs) and galaxies still need to be understood. It has been proposed that highly ionised gas outflows could play a pivotal role in this process (e.g. King 2003, 2005; Gaspari & Sądowski 2017). The presence of such powerful winds is expected to regulate accretion of material onto (and ejection from) compact objects.

Through their mechanical power, ultra-fast outflows (UFOs) are accelerated at velocities greater than $10\,000\,{\rm km\,s^{-1}}$ and up to a few dozen times the speed of light. For these reasons, UFOs are also able to inject momentum and energy over wide spatial scales via interaction with the interstellar medium (ISM) in the host galaxy. This process is expected to promote an efficient

feedback mechanism (e.g. Murray et al. 2005; Di Matteo et al. 2005; Ostriker et al. 2010; Torrey et al. 2020), which is needed to reproduce the observed properties in galaxies, for example the scaling relations (King et al. 2011), and to regulate their overall mass-size ecosystem (e.g. Fabian 2012; King & Pounds 2015; Heckman & Best 2014).

Ultra-fast outflows are routinely detected in the X-ray spectra of 30–40% of local ($z \lesssim 0.1$) AGNs (Tombesi et al. 2010; Gofford et al. 2013; Igo et al. 2020, hereafter T10; G13; Igo20), and in a handful of sources at intermediate to high redshifts (up to $z \sim 3$; e.g. Chartas et al. 2002; Lanzuisi et al. 2012; Chartas et al. 2021, hereafter C21). They manifest themselves as absorption troughs associated with Fe XXV Heα and Fe XXVI Lyα transitions ($E_{\rm rest} = 6.7$–6.97 keV) blueshifted at energies $E_{\rm rest} > 7$ keV (all the line energies will be given in the source rest frame throughout this work). The degree of blueshift translates into the range of extreme outflow velocities observed from $v_{\rm out} \sim -0.03c$ up to $-0.5c$, for gas column densities and ionisations of $N_{\rm H} \sim 10^{23-24}\,{\rm cm^{-2}}$ and $\log(\xi/{\rm erg\,cm\,s^{-1}}) \gtrsim 3$, respectively (e.g. Reeves et al. 2003, 2018a; Pounds & Reeves 2009; Tombesi et al. 2011; Matzeu et al. 2017; Parker et al. 2018; Braito et al. 2018). The frequent detection of these features, supported by a detailed modelling of the high energy spectra of the most powerful local quasar (QSO) to host X-ray winds, PDS 456, indicates that UFOs arise in wide angle outflows,

in turn implying that a significant amount of kinetic power is involved (Nardini et al. 2015; Luminari et al. 2018).

Evidence for low-ionisation UFO components has also been reported in the soft X-ray spectra in the $E_{\rm rest}$ = 0.3–2 keV band (e.g. Braito et al. 2014; Longinotti et al. 2015; Reeves et al. 2016, 2018b, 2020; Serafinelli et al. 2019; Krongold et al. 2021), usually observed as blueshifted oxygen and neon ions. Similar high-velocity outflows, arising directly from the accretion disc region, have also been found in the UV spectra via prominent blueshifted, ionised absorption, and emission features in broad absorption line QSOs, typically between $\lambda_{\rm rest}$ = 50 and 2000 Å (e.g. Gaskell 1982; Wilkes & Elvis 1987; Richards et al. 2011). They are associated with lower-ionisation metal ions (C IV, Al II, Fe II, etc.; e.g. Crenshaw et al. 2003; Green et al. 2012; Hamann et al. 2018; Kriss et al. 2018, 2019; Mehdipour et al. 2022; Vietri et al. 2022). It has been shown that at least some of the UV-absorbing outflows in sub-Eddington systems can be driven by radiation pressure on spectral lines (e.g. Murray et al. 1995; Proga et al. 2000). We refer readers to the recent review by Giustini & Proga (2019) for more details.

Outflowing material at considerably lower velocities (typically within a $v_{\rm out}$ of −5000 km s^{-1}) and less ionised than UFOs at $\log(\xi/\mathrm{erg\,cm\,s^{-1}}) \sim 1-3$ (e.g. Sako et al. 2000; Parker et al. 2019), known as a warm absorber (WA), is also detected through absorption features and edges from He- and/or H-like ions of C, O, N, Ne, Mg, Al, Si, and S in X-rays (Halpern 1984; Mathur et al. 1997, 1998; Blustin et al. 2005; Reeves et al. 2013; Kaastra et al. 2014; Laha et al. 2014, 2016). Warm absorbers are detected in a substantial fraction of AGNs: ~65% (Reynolds 1997; Piconcelli et al. 2005; McKernan et al. 2007). It was suggested by Tombesi et al. (2013) that, despite their physical distinction, UFOs and WAs might be somehow connected as part of the same wind, but originating from different locations (see Laha et al. 2021 for a comprehensive review of ionised outflows).

Finally, outflowing gas is also routinely observed at host-galaxy scales, in the ionised, neutral and molecular phases. These outflowing components observed at kiloparsec scales or beyond are now traced with modern sensitive optical/far-IR/millimetre/radio facilities (e.g. Morganti et al. 2005; Feruglio et al. 2010, 2017; Harrison et al. 2014; Brusa et al. 2015, 2018; Maiolino et al. 2012; Cresci et al. 2015; Bischetti et al. 2019a) and show lower velocities with respect to the accretion disc winds ($v_{\rm out}$ ~ −500 to −2000 km s^{-1}, depending on the phase) and considerably higher mass outflow rates of up to 100–1000 $M_\odot$ yr^{-1} (see Cicone et al. 2018).

Some models predict that the fast outflowing gas is accelerated by the radiation pressure caused by highly accreting black holes approaching the Eddington limit (e.g. Zubovas & King 2012). Subsequently, the energy deposited via shocks by the UFO into the galaxy ISM generates the galaxy-wide outflows observed in lower-ionisation gas (see Fabian 2012; King & Pounds 2015). Alternatively, massive sub-relativistic outflows are also expected in systems accreting at a lower Eddington ratio, due to magnetic (e.g. Fukumura et al. 2010, 2017; Kraemer et al. 2018) and/or thermal driving (e.g. Woods et al. 1996; Mizumoto et al. 2019; Waters et al. 2021). The global AGN feeding-feedback self-regulated framework has been supported by three-dimensional hydrodynamical simulations that unify the micro and macro properties of the AGN environment (e.g. Gaspari et al. 2013, 2020; Sądowski & Gaspari 2017; Yang et al. 2019; Wittor & Gaspari 2020); these simulations have, in turn, been corroborated by several multi-

wavelength observations (e.g. Maccagni et al. 2021; Eckert et al. 2021; McKinley et al. 2022; Temi et al. 2022).

Multi-phase tracers would therefore allow us to probe galactic outflows in their full extent, that is, from the nuclear (<1 pc) to the largest scales (>10 kpc), and at the same time provide us with a comprehensive view of their driving mechanism. Fiore et al. (2017) reported a correlation between the velocity of the wind (for both UFOs and large-scale components) and the bolometric luminosity ($L_{\rm bol} \propto v_{\rm out}^{3.9}$), in agreement with that predicted by Costa et al. (2014) for energy-conserving outflows. However, the statistics of this work for the UFO sample are still limited (~20 AGNs with UFOs), with only 50% at $L_{\rm bol} \gtrsim 10^{45}$ erg s^{-1}.

A comparison between the momentum rates (i.e. $\dot{p}_{\rm out} = \dot{M}_{\rm out} v_{\rm out}$) observed over a range of spatial scales can be used to disentangle the wind propagation mechanisms: energy-conserving (large-scale) versus momentum-conserving (small-scale: UFO). The first reported cases of molecular outflows in systems that host a UFO were IRAS F11119+3257 (Tombesi et al. 2015), Mrk 231 (Feruglio et al. 2015), IRAS 17020+4544 (Longinotti et al. 2015, 2018), and APM 08279+5255 (Feruglio et al. 2017). These examples support the energy-driven wind scenario, deemed as the smoking gun for large-scale feedback. Indeed, conserving energy is crucial for achieving an effective macro-scale feedback to quench cooling flows and star formation (e.g. Gaspari et al. 2019). However, via the analysis of more sources, it emerged that not all outflows supported this scenario. Further molecular outflows observed in UFOs that host sources, such as PDS 456 (Bischetti et al. 2019b), MCG–03–58–007 (Sirressi et al. 2019), I Zwicky 1 (Cicone et al. 2014; Reeves & Braito 2019), and Mrk 509 (Zanchettin et al. 2021), revealed momentum rates at least two orders of magnitude below the expected value for an energy-conserving wind (see also Marasco et al. 2020; Tozzi et al. 2021). These results suggest a more complex physical mechanism and range of efficiencies in transferring the nuclear wind out to the large-scale galaxy structure, or significant AGN variability over the lifetime of the flow (Nardini & Zubovas 2018; Zubovas & Nardini 2020), as supported by chaotic cold accretion simulations (Gaspari et al. 2017). Related to this, an important parameter that is needed to constrain wind models is the UFO duty cycle, that is, how persistent accretion disc winds are. Indeed, the derivation of the energy injection rate by UFOs into the galaxy ISM must take this factor into account, with implications for the timescale and efficiency of propagation through the host galaxy (Zubovas & King 2016). The UFO duty cycle can be inferred from the fraction of AGNs in which they are observed, but it is highly degenerate with the opening angle. Hence, as of today, it is virtually unconstrained for sources above $L_{\rm bol}$ ~ 10^{45} erg s^{-1}. Observing large samples of sources at luminosities above the break $L \gtrsim L^\star$ of the AGN luminosity function (e.g. Aird et al. 2015), with a range of Eddington ratios and enough statistics to constrain the wind duty cycle, has become crucial for overcoming the limitations described above (e.g. Bertola et al. 2020).

This work is the first in a series of Supermassive Black Hole Winds in the X-rays (SUBWAYS) publications. The SUBWAYS programme has the dedicated goals of investigating the various manifestations of UFOs emanating from the environments of SMBHs in AGNs. This includes gaining significant advances in our understanding of the detection rate and physical properties of UFOs, their connection with WA features, and their role in providing a macro-scale feedback, as well as mapping the physical properties of the outflows across different galaxy scales

and gas phases at different wavelengths and ionisation states. In this paper we present our first results of the SUBWAYS campaign, specifically designed to provide a solid detection of blueshifted absorption features in the Fe K band in the context of robust statistical grounds for high signal-to-noise ratio (S/N) sources at $L \gtrsim 10^{45}\,\mathrm{erg\,s^{-1}}$.

The paper is organised as follows: Sect. 2 presents the SUBWAYS sample and the target selection. In Sect. 3 we describe the reduction of the X-ray Multi-Mirror mission (*XMM-Newton*) data. In Sect. 4 we present all the details of the spectral analysis of the European Photon Imaging Camera (EPIC) data, including the continuum modelling, the procedure we adopted to search for Fe K emission and absorption features, the modelling of the Fe K band, and the Monte Carlo ($\mathcal{MC}$) simulations we used to assign a robust significance level to the detections. In Sect. 5 we present our main results, namely the line detection rate as inferred from our spectral modelling, and in Sect. 6 we discuss our findings in light of recent results at both lower and higher redshifts; Sect. 7 summarises our results. Cosmological values of $H_0 = 70\,\mathrm{km\,s^{-1}\,Mpc^{-1}}$, $\Omega_{\Lambda_0} = 0.73$, and $\Omega_M = 0.27$ are assumed throughout this paper, and errors are quoted at the 90% confidence level or a difference in C-statistic (i.e. $\Delta C = 2.71$; Cash 1979) for one parameter of interest, unless otherwise stated. The cosmic abundances are set to solar throughout the paper.

2. The SUBWAYS campaign

So far, the characterisation of the fastest components of accretion disc winds has mainly been carried out through studies based on inhomogeneous archival data, restricted to two distinct cosmic epochs and luminosity regimes, merely for practical reasons: (i) at $z < 0.1$, objects are close enough that it is relatively easy to collect $>5-10 \times 10^3$ counts in the 4–10 keV band in large samples (~50 objects), but mainly limited to Seyfert luminosities ($L_{bol} \lesssim 10^{45}\,\mathrm{erg\,s^{-1}}$; e.g. T10; G13; Igo20); (ii) at $z \gtrsim 1.5$, on small and sparse samples (<10 objects) at $L_{bol} \gtrsim 10^{46}\,\mathrm{erg\,s^{-1}}$, which are mostly composed of gravitationally lensed objects (e.g. Chartas et al. 2009; Vignali et al. 2015; Dadina et al. 2016, C21). The distribution of these two samples in the L–z plane is shown in the upper panel of Fig. 1 (blue and magenta points, respectively).

In order to gain significant advances in our understanding of the physical properties of UFOs in the QSO-like regime, a systematic approach is needed. The SUBWAYS sample consists of a total of 22 radio-quiet X-ray AGNs, mostly Type 1 and QSOs, where 17 sources have been observed with *XMM-Newton* (Jansen et al. 2001) between May 2019 and June 2020 (see Table 1) as part of a large programme (1.45 Ms, PI: M. Brusa) awarded in 2018 (cycle AO18 LP). In addition, the sample includes the data of five sources that meet the L–z–counts selection criteria (see below) already available in the archive[1]. A companion SUBWAYS paper, Paper II (Mehdipour et al. 2023), is primarily focused on the UV outflow spectroscopic analysis of Cosmic Origins Spectrograph (Green et al. 2012) data as part of a large complementary SUBWAYS observational campaign carried out with the *Hubble* Space Telescope.

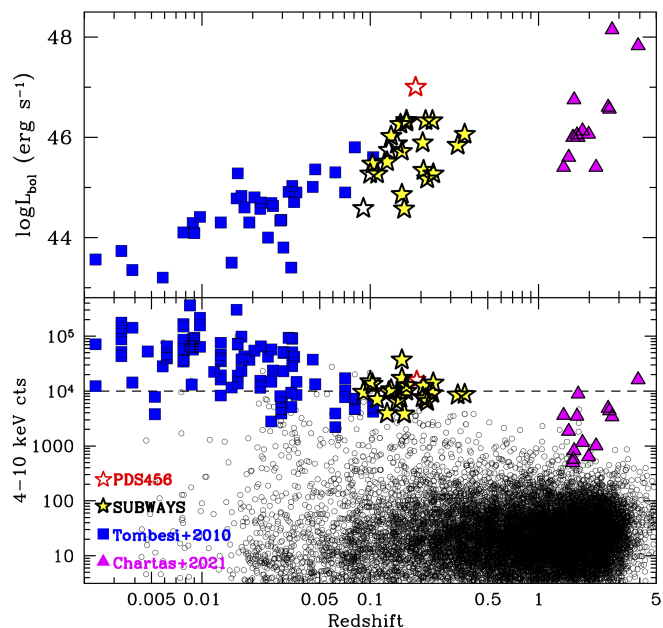The SUBWAYS selection criteria are based on the following requirements. Firstly, The presence of the source in

---

[1] In this analysis we discarded all observations with a net count threshold of $\lesssim 1500$ in the 4–10 keV band.

Fig. 1. Luminosity (upper panel) and rest-frame 4–10 keV counts (lower panel) plotted against redshift for the objects in the SUBWAYS sample and the comparison samples (T10; C21), as labelled. In the lower panel we also mark the sources of the 3XMM sample, used to select the SUBWAYS targets, with small empty circles.

the 3XMM-DR7 catalogue[2], matched to the SDSS-DR14 catalogue[3], or to the Palomar-Green Bright QSO catalogue (PGQSO; Schmidt & Green 1983). Secondly, an intermediate redshift in the range, $z = 0.1$–0.4. This condition ensures that both WAs and UFOs can be studied at the same time, and provides the possibility to characterise the continuum up to 10 keV. Indeed, in order to recognise faint absorption features, it is key to achieve a good handling of the continuum in spectra with high counting statistics up to 10 keV. Thirdly, a count rate larger than ~0.12 cts/s, in order to ensure counts of the order of ~10^4 in the 4–10 keV band in the EPIC-pn spectra, obtained within a single *XMM-Newton* orbit. A by-product of this requirement also implies that our targets are QSOs ($L_{bol} \gtrsim 10^{45}\,\mathrm{erg\,s^{-1}}$; star points in Fig. 1), complementing the data already available in the archives for this kind of studies. Lastly, we discarded narrow-line Seyfert 1 galaxies (NLSy1s) due to the highly variable EPIC count rate, and QSOs in clusters/radio loud systems, in order to avoid contamination by processes other than AGN accretion and UFOs.

The lower panel of Fig. 1 shows the currently available rest-frame 4–10 keV counts for the SUBWAYS sample (large stars), compared to those in 3XMM-SDSS, 3XMM-PGQSO, and local and high-z QSO UFO samples (see the labels and caption for details). In this paper we focus specifically on the detection and characterisation of blueshifted absorption profiles in the Fe K band in the 17 newly observed sources plus the additional 5 from previous observations (up to AO18 cycle), for a total of 22 targets. The properties of the targets are listed in Table 1.

3. Data reduction

In this work we focus on the EPIC-pn (Strüder et al. 2001), EPIC-MOS 1, and MOS 2 (Turner et al. 2001) data. They were

---

[2] http://xmmssc.irap.omp.eu/Catalogue/3XMM-DR7/3XMM_DR7.html

[3] https://skyserver.sdss.org/dr14/en/home.aspx

Table 1. Target properties of the large SUBWAYS campaign.

Name (1)	z (2)	$N_{\rm H}^{\rm Gal}$ (3) $(10^{20} \, {\rm cm}^{-2})$	$\log L_{\rm X}$ (4) $({\rm erg \, s}^{-1})$	$\log L_{\rm bol}$ (5) $({\rm erg \, s}^{-1})$	$\log M_{\rm BH}$ (6) $(M_\odot)$	$\log L_{\rm bol}/L_{\rm Edd}$ (7)	$\log F_{2-10\,{\rm keV}}$ (8) $({\rm erg \, cm}^{-2} \, {\rm s}^{-1})$
PG0052+251	0.15445	3.96	44.609 ± 0.003	46.00	8.41 [a]	−0.51	-11.204 ± 0.003
PG0953+414	0.23410	1.09	44.595 ± 0.004	46.08	8.24 [a]	−0.26	-11.664 ± 0.004
PG1626+554	0.13170	1.55 [†]	44.076 ± 0.004	45.42	8.54 [a]	−1.22	-11.600 ± 0.004
PG1202+281	0.16501	1.74	44.400 ± 0.004	45.77	8.61 [a]	−0.94	-11.469 ± 0.004
PG1435−067	0.12900	4.84	43.684 ± 0.007	44.98	7.77 [b]	−0.89	-11.962 ± 0.007
SDSSJ144414+0633	0.20768	2.57	44.467 ± 0.004	45.84	8.10 [c]	−0.36	-11.634 ± 0.004
2MASXJ165315+2349	0.10300	4.15	43.790 ± 0.006	45.37	6.98 [e]	0.29	-11.529 ± 0.007
PG1216+069	0.33130	1.51	44.769 ± 0.004	46.24	9.20 [a]	−1.06	-11.810 ± 0.005
PG0947+396 (Obs1)	0.20553	1.91 [†]	44.208 ± 0.007	45.55	8.68 [a]	−1.24	-11.887 ± 0.008
PG0947+396 (Obs2)	0.20553	1.91 [†]	44.146 ± 0.006	45.55	8.68 [a]	−1.24	-11.954 ± 0.007
WISEJ053756−0245	0.11000	15.0	43.688 ± 0.005	44.86	7.73 [e]	−0.97	-11.777 ± 0.006
HB891529+050	0.21817	3.93	44.219 ± 0.005	45.52	8.75 [c]	−1.33	-11.918 ± 0.005
PG1307+085	0.15384	2.10	44.312 ± 0.003	45.70	7.90 [a]	−0.30	-11.512 ± 0.003
PG1425+267	0.36361	1.57	44.823 ± 0.004	46.31	9.22 [c]	−1.01	-11.823 ± 0.005
PG1352+183	0.15147	1.55	43.889 ± 0.004	45.21	8.42 [a]	−1.31	-11.921 ± 0.005
2MASXJ105144+3539 [e]	0.15900	2.20	43.692 ± 0.008	44.88	8.40 [c]	−1.62	-12.068 ± 0.009
2MASXJ0220−0728	0.21343	2.42	44.213 ± 0.005	45.51	8.42 [e]	−1.01	-11.888 ± 0.006
LBQS1338−0038	0.23745	1.68	44.520 ± 0.003	45.91	7.77 [c]	0.04	-11.707 ± 0.004
				Archival targets			
PG0804+761 [d]	0.10000	7.09	44.330 ± 0.002	45.71	8.31 [d]	−0.33	-11.087 ± 0.003
PG1416−129	0.12900	3.34	44.170 ± 0.005	45.58	9.05 [a]	−1.57	-11.447 ± 0.005
PG1402+261	0.16400	1.22	44.030 ± 0.004	45.39	7.94 [a]	−0.65	-11.874 ± 0.004
HB89 1257+286	0.09100	1.04	43.551 ± 0.002	45.15	7.46 [c]	−0.41	-11.831 ± 0.002
PG1114+445	0.14400	1.93 [†]	44.088 ± 0.003	45.53	8.59 [a]	−1.16	-11.602 ± 0.003

Notes. (1) Target name; (2) Redshift; (3) Galactic absorption measured by HI4PI Collaboration (2016) or Murphy et al. (1996)[†]; (4) 2–10 keV intrinsic luminosity measured in this work by using the clumin convolution model in XSPEC; (5) bolometric luminosity derived from the X-ray luminosity assuming the bolometric correction of Duras et al. (2020); (6) log of black hole mass from the measurements carried out in Bianchi et al. (2009)[a], Xie et al. (2017)[b], Perna et al. (2017)[c], Kaspi et al. (2000b)[d] and this work[e]; (7) Eddington ratio; (8) 2–10 keV fluxes from the available spectra measured with cflux in XSPEC. The $L_{\rm X}$ and $L_{\rm bol}$ measured in this work are consistent with the ones that were used during the SUBWAYS selection process.

processed and cleaned by adopting the Science Analysis System SAS v18 (Gabriel et al. 2004) and the up-to-date calibration files. We initially checked for Cu instrumental emission in the EPIC-pn CCDs, between 7–8.5 keV and 7.8–8.2 keV, for the source extraction and subsequent high-background screening. We followed the Piconcelli et al. (2004) optimised procedure aimed at maximising the S/N in the 4–10 keV band (in the EPIC-pn), rather than using the conservative criterion based on the fiducial rejection of time-intervals of high-background count rates (i.e. between 10–12 keV). The S/N optimisation procedure is necessary to identify any absorption feature that would otherwise be diluted (e.g. Nardini et al. 2019), but insufficient if this does not also correspond to the optimal compromise between S/N and number of counts (see Fig. 2).

Given the relatively small EPIC-MOS collecting area at $E_{\rm obs} \geq 4$ keV, a 4–10 keV band optimisation would remove too many counts; we then optimised the filtering on the entire 0.3–10 keV band. Apart from the different reference bands, the applied method is the same for the pn and MOS instruments. We selected a background region free of instrumental features. These regions have dimensions of 40 or 50 arcsec depending on the possibility, for each observation, to find source-free regions on the detectors. In order to define the source regions different extraction radii were tested and for each radius we calculated the maximum level of background that can be tolerated in order to find the optimal S/N. Following Piconcelli et al. (2004), we define this level of background as the max background (see

Appendix A for more details). The EPIC source spectra were individually inspected for the possible presence of photon pile-up by using the SAS task EPATPLOT. The ratios of singles to double pixel events were found to be within 1% of the expected nominal values, and thus no significant pile-up is present. The response files were subsequently generated with the SAS tasks RMFGEN and ARFGEN with the calibration EPIC files version v3.12. In Table B.1 we show a summary of the individual observations of the 22 SUBWAYS targets that were selected adopting a threshold of ≥1500 EPIC-pn net counts in the 4–10 keV band.

4. Spectral analysis

The pioneering UFO studies were conducted on large archival samples of AGNs. More specifically, T10 carried out a systematic hard-band (i.e. 3.5–10.5 keV) analysis on a sample of 42 sources (for a total of 101 observations), drawn from the archival *XMM-Newton* EPIC data, to carry out a blind search of Fe XXV Heα and Fe XXVI Lyα absorption lines. By analysing the data of 51 AGNs, obtained with the *Suzaku* observatory, G13 constructed broadband spectral models over the entire band pass (i.e. 0.6–10 keV).

For a robust analysis, we chose, as per G13, the entire EPIC band pass, where additional spectral complexities like WAs and/or strong soft excesses can also be taken into account. In this way we ensure that all our models accurately describe the overall continuum. We focus on the *XMM-Newton* EPIC-pn, MOS 1,
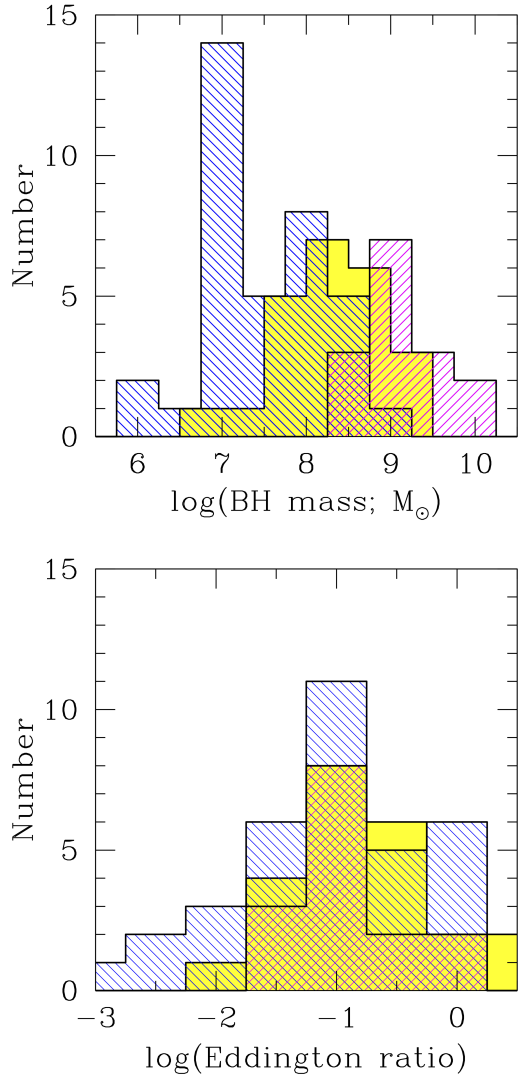
Fig. 2. Black hole mass and Eddington ratio distributions of our targets (see Table 1) and the comparison samples. The colour scheme for the samples is the same as in Fig. 1.

and MOS 2 data in the 0.3–10 keV range. We applied a blind-search procedure in each of the 41 observations by adopting four spectral binning methods (for a total of 164 blind-searches; see Appendix C for details). These binnings are `grpmin1`, `SN5`, and `OS3grp20`, using the `SAS` routine `SPECGROUP`, and the optimal binning of Kaastra & Bleeker (2016, $\mathcal{KB}$ hereafter), using the `HEASOFT` routine `FTGROUPPHA`.

We find that the spectral resolution delivered by the `SN5` and `OS3grp20` binning methods is too degraded compared to the `grpmin1` and $\mathcal{KB}$ ones, and therefore not suitable for the detection of faint, narrow absorption and emission features. The `grpmin1` and $\mathcal{KB}$ criteria produce nearly identical results, in terms of detection rate and statistical significance of the features. While `grpmin1` would certainly be a more conservative option, we finally chose the $\mathcal{KB}$ binning, which is specifically developed to optimise the S/N in narrow, unresolved spectral features whilst maintaining the necessary spectral resolution. Such a choice provided the right compromise between these binning methods. In other words, Kaastra & Bleeker (2016) worked out a binning scheme based on the resolution of the detector and the available number of photons at the energy of interest. Such

a method allowed us to maximise the information provided by the Fe K absorption lines, and in this framework we adopted a maximum likelihood statistic as C−stat.

4.1. Continuum modelling

All the spectra were initially fitted with a power law and their corresponding Galactic absorption, modelled with `Tbabs` (Wilms et al. 2000), with column densities obtained from the HI4PI Collaboration (2016) survey. In order to accurately parameterise the properties of the underlying continuum, additional model components were required in the process such as warm or neutral absorption, or a soft excess, as outlined in Sects. 4.1.1 and 4.1.2.

We note that statistically identical results could have been achieved by modelling the continuum with distant and/or ionised Compton reflection models such as `xillver` (García et al. 2013) or `relxill` (Dauser et al. 2014; García et al. 2014). Since the *XMM-Newton* band pass is 0.3–10 keV, the contribution from the Compton reflection continuum is not well constrained; therefore, for simplicity, here we adopt a power-law plus blackbody (when required) parameterisation of the continuum. A similar approach was also adopted in the Catalogue of AGN in the *XMM-Newton* Archive (CAIXA) sample by Bianchi et al. (2009). Nonetheless, a thorough investigation using Compton and relativistic reflection models is addressed in a forthcoming companion paper, where we take advantage of the Nuclear Spectroscopic Telescope Array mission (*NuSTAR*) follow-up obtained in 2020 (PI: Bianchi).

Our baseline phenomenological model can be described as

$$\texttt{Tbabs} \times \texttt{XABS} \times (\texttt{zbbody}_1 + \texttt{zbbody}_2 + \texttt{powerlaw}), \qquad (1)$$

where `Tbabs` represents the absorption due to our Galaxy, `powerlaw` accounts for the primary emission component, and $\texttt{zbbody}_{1,2}$ are two layers of blackbody emission to account for the soft X-ray excess[4]. This parameterisation of the soft excess is only phenomenological and hence the corresponding temperatures are not meaningful. `XABS` (when required) corresponds to a mildly ionised warm absorption component (see Sect. 4.1.1).

Once the best fit of the 0.3–10 keV continuum spectra of each of the 41 observations was reached, we performed a systematic search for iron K emission and absorption profiles between 4–10 keV using the following two methods: (i) blind-line search via energy–intensity plane contours plots (Sect. 4.2) and (ii) extensive $\mathcal{MC}$ (e.g. Protassov et al. 2002) simulations (Sect. 4.4). The modelling approach of each individual spectral component is described below and the detailed continuum and absorption parameters are tabulated in Table D.1

4.1.1. Intrinsic absorption

Neutral or lowly ionised absorption is typically constituted by a distant ($\gtrsim$pc scales), less ionised and denser circumnuclear material compared to UFOs, generally outflowing at velocities in the range of ~ -100 to -1000 km s^{-1} (e.g. Kaastra et al. 2000; Kaspi et al. 2000a; Blustin et al. 2005). These absorbers are detected in the soft X-ray part of the spectrum at energies $\lesssim 2$–3 keV and, depending on their properties, they can add a significant curvature to the spectra below 10 keV

---

[4] In some SUBWAYS targets only one blackbody component is required (see Sect. 4.1.2), while no blackbody component is needed for the absorbed sources 2MASS J105144+3539 and 2MASS J165315+2349.

(e.g. Matzeu et al. 2016; Boller et al. 2021), and hence affect the overall continuum and line parameters in our broadband models. In the literature, the fraction of sources with reported WAs is >60% (Tombesi et al. 2013; G13).

In 2MASS J105144+3539, an intrinsic neutral absorption column of $N_{\rm H} = 6.7 \pm 0.4 \times 10^{21}\,{\rm cm}^{-2}$ and two emission lines in the soft band, likely associated with collisionally ionised gas, are required. 2MASS J165315+2349 is classified as a Seyfert 2 and so requires a different model construction in the soft X-rays, with the presence of an intrinsic neutral absorber and emission arising from a distant scattered component. The continuum model differs from Eq. (1) as

$$\texttt{Tbabs} \times (\texttt{powerlaw}_{\rm scatt} + \texttt{apec}_1 + \texttt{apec}_2 + \texttt{phabs} \times \texttt{powerlaw}_{\rm intr}),\tag{2}$$

where $\texttt{apec}_{1,2}$ (Smith et al. 2001) are thermal models accounting for two regions of emitting collisionally ionised plasma and $\texttt{powerlaw}_{\rm scatt}$ reproduces the distant scattered component. $\texttt{powerlaw}_{\rm intr}$ accounts for the primary continuum, which is absorbed by fully covering neutral material (phabs) with a column density of $N_{\rm H} = 2.2 \pm 0.9 \times 10^{23}\,{\rm cm}^{-2}$.

In this work we model the presence of fully covering mildly ionised absorption with a specifically generated XABS model from SPEX (Kaastra et al. 1996; Steenbrugge et al. 2003) converted to an XSPEC (Arnaud 1996) table[5] (see the appendix of Parker et al. 2019). More specifically the XABS table covers the following ranges in the parameter space: column density in the range $10^{20} \leq N_{\rm H}/\,{\rm cm}^{-2} \leq 10^{22}$ with 10 logarithmic steps, and ionisation in the range $-4 \leq \log(\xi/{\rm erg\,cm\,s}^{-1}) \leq 6$ with 20 linear steps, making this table well suited for investigating a wide range of absorbers in AGNs such as WAs. Although the presence of WAs could have a minimal effect on the Fe K region, we find it essential to include them as the most reliable continuum level must be determined.

The XABS table was generated by assuming the default SPEX setting where the spectral energy distribution (SED) of NGC 5548 was used as representative of a standard AGN input spectrum[6] (see Steenbrugge et al. 2005, for more details). Another parameter in the model is the two-dimensional root mean square velocity ($v_{\rm rms}$), which gives a measure of the velocity dispersion of the line profile[7]. At the energy resolution of the EPIC CCDs (see Appendix C), the individual soft X-ray absorption lines are indeed unresolved, so in the fitting procedure the RMS velocity broadening was frozen to its default value, $v_{\rm rms} = 100\,{\rm km\,s}^{-1}$ (unless specified otherwise), and the systemic velocities were set to $0\,{\rm km\,s}^{-1}$.

Here we also consider the possibility of partial covering along the line of sight. In this regime a fraction corresponding to $f_{\rm cov} < 1$ of the total flux is indeed absorbed, while a portion $1 - f_{\rm cov}$ leaks through the absorbing layer. This can also have a dramatic effect on the emerging continuum by imprinting a prominent spectral curvature at energies <10 keV (e.g.

Matzeu et al. 2016; Boller et al. 2021). On this basis a partial covering fraction was also added to the list of free parameters in our XABS table (i.e. $0 \leq f_{\rm cov} \leq 1$). A more comprehensive physical analysis of low- and high-ionisation outflows is presented in a companion paper.

4.1.2. The soft excess

The soft X-ray excess is described as a strong featureless emission component that is often observed in unabsorbed AGNs below ~2 keV. The physical mechanism responsible for this emission is still the subject of active debates; it may be a dual-coronal system (e.g. Done et al. 2012; Petrucci et al. 2013, 2018; Różańska et al. 2015; Middei et al. 2018; Ursini et al. 2020; Ballantyne & Xiang 2020; Porquet et al. 2021) or relativistic blurred reflection (e.g. Ross & Fabian 2005; Nardini et al. 2011; Wilkins & Fabian 2012; Walton et al. 2013; García et al. 2019; Jiang et al. 2019; Xu et al. 2021; Mallick et al. 2022).

Regardless of the physical origin of the soft excess, in this work we take a completely empirical approach by fitting its profile with one/two layers of blackbody emission, when required at the $\Delta C/\Delta \nu \gtrsim 9.3/2$ threshold (i.e. ≳99% confidence level for each blackbody component) in XSPEC (e.g. Porquet et al. 2004a; Piconcelli et al. 2005; Bianchi et al. 2009, G13). Although our phenomenological model largely ignores the detailed physics involved in the system, it allows us to fit and compare uniformly the underlying continua in our sample so that we can concentrate on the Fe K band. There might be some degeneracies between the soft excess and partial covering components during fitting; however, this is not an issue for our absorption line detections. We could have modelled equally well the soft excess with a reflection component and the final result would not change, as discussed above in Sect. 4.1.

4.2. Search for Fe K emission and absorption

In Fig. 3 (top) we report, as an example, the background-subtracted *XMM-Newton* spectra (EPIC-pn, black; EPIC-MOS 1, red; EPIC-MOS 2, green) and their corresponding background spectra of PG 0052+251. This source is one of the most luminous in the sample and is on the bright side of the luminosity/counts distribution in Type 1 AGNs (see Fig. D.1).

The 0.3–10 keV (rest-frame) best-fitting broadband continuum model (excluding iron K emission and/or absorption lines) is indicated in solid-red. The residuals are shown in the bottom panel. Our baseline continuum models include the absorbed power-law component and the two blackbody components, with high and low temperatures (kT). The continua are well reproduced with our baseline model (see the model statistics reported in Table D.1). Two exceptions were found in the sample: when the soft X-ray emission was parameterised with one or two regions of collisionally ionised plasma modelled with $\texttt{apec}$ in 2MASS J105144+3539 and 2MASS J165315+2349, respectively. The presence of strong residuals from neutral Fe Kα core emission at $E_{\rm rest} = 6.4$ keV from distant material is ubiquitous in the SUBWAYS sample (e.g. see Fig. 3).

In some observations (see Fig. D.1) we observed strong absorption residuals (also in the Fe K band) likely associated with Fe XXV–Fe XXVI transitions. Therefore, we ran a blind search, simultaneously in both EPIC-pn and EPIC-MOS spectra for every observation in the sample, in order to have a first assessment of energy, strength, shape and significance of any absorption or emission line relative to the underlying

---

[5] https://www.michaelparker.space/xspec-models

[6] We are aware that our XABS table is built based on the ion balance calculated for a typical Seyfert, while our sample consists of QSOs of higher luminosity. By testing the same data with an XSTAR grid with turbulent velocity of $v_{\rm turb} = 300\,{\rm km\,s}^{-1}$ and a power-law SED input with a photon index of $\Gamma = 2$, we get ionisation parameters that are slightly higher but consistent within the errors. For this reason, we allowed ξ to explore the wide range of ionisation reported above.

[7] https://personal.sron.nl/~jellep/spex/manual.pdf

continuum model. We performed an inspection of the deviation in $|\Delta C|$ from the best-fitting continuum model by generating two-dimensional energy–intensity contours plots. This method was adopted by T10 and G13, and extra details are described in Miniutti & Fabian (2006).

The search was performed with our baseline continuum model (Eqs. (1) or (2)) plus a narrow Gaussian line (with the velocity width fixed at $\sigma_{\text{width}} = 10$ eV). We also let the power-law photon index and normalisation free to vary during the search. In adopting our broadband 'multi-component' continuum model above, we ensure a better reproduction accuracy of the continuum level compared to a simpler two-component power law plus Gaussian line model restricted on the Fe K band. For this routine we freeze all the soft X-rays parameters from the broadband continuum to their best-fit values, re-fit, and run the scan along with the 5–10 keV, rest-frame energy band. The blind search method adopted here is carried out based on the following steps: (i) We have a baseline continuum model between 0.3–10 keV (described above) plus the unresolved Gaussian line required for the scan. The Fe Kα emission line at 6.4 keV was not included in the baseline model. For each run, the energy of the Gaussian is scanning the three EPIC spectra simultaneously between 5–10 keV in intervals of $\Delta E = 50$ eV. The normalisation of the Gaussian component probes the intensity of the spectral line and is free to vary between negative and positive values in 250 steps. (ii) Each individual step in the energy–intensity plane with respect to the baseline model was recorded into a file including the corresponding ΔC. (iii) The resulting confidence contours are plotted according to a mapped ΔC deviation of -2.3, -4.61, -9.21, -13.82 and -18.52 for 2 parameters of interest corresponding to the nominal 68%, 90%, 99%, 99.9% and 99.99% confidence levels. (iv) We inspect the contour plots to check whether there is any evidence of emission and/or absorption in the spectrum (see the text below).

If an emission or absorption line is detected, it is parameterised by using a Gaussian profile. All the key Gaussian absorption and emission parameters accounting for the detected lines, using the $\mathcal{KB}$ binning, are tabulated in Table 2. The ΔC mapping provided by the energy–intensity contours is a powerful tool to detect emission or absorption profiles by visually assessing the location and strength of the line relative to the underlying continuum model. The spectral complexity within the 5–10 keV band can be enhanced by a number of atomic features such as ionised emission lines from Fe XXV and Fe XXVI, at 6.7 keV and 6.97 keV, respectively. As we have learned from previous work, in ultra-fast wind systems the ionised emission due to scattered photons from the outflowing material can be as important as the absorption (e.g. Sim et al. 2008; Nardini et al. 2015; Luminari et al. 2018; Matzeu et al. 2022). In several SUBWAYS spectra, the shape of the emission and/or absorption profiles is indeed complex/broad, which suggests a superposition/blending of multiple ionised lines. Steps (i)–(iv) were carried out in each fitted EPIC spectrum of the sample.

Examples of this method are shown in Fig. 4. In the top panel we show the corresponding residual of EPIC-pn spectrum (MOS 1 and MOS 2 are not included for clarity) without the emission and absorption components. The vertical dashed lines denote the position of the laboratory energy transition of Fe Kα (lime green), Fe XXV (magenta) and Fe XXVI (magenta).

In Fig. 4 we show the result of the same blind-search procedure applied to the type 1 AGN LBQS 1338−0038. The energy–intensity contour map is showing the presence of highly significant emission and absorption profiles at centroid rest-frame energies of $E_{\text{em}} \sim 6.6$ keV and $E_{\text{abs}} \sim 8$ keV, respectively. What
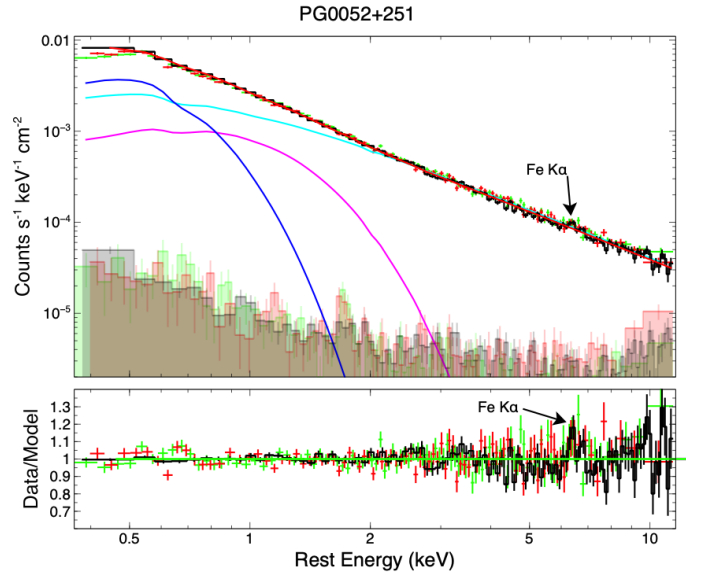

Fig. 3. Broadband EPIC data and best-fit continuum of PG 0052+251 between the rest-frame energy of 0.3–10 keV. Top: background-subtracted *XMM-Newton* spectra (EPIC-pn in black, EPIC-MOS 1 in red, EPIC-MOS 2 in green) and their corresponding background levels (shaded areas). The broadband best-fit continuum model (solid red) is shown alongside the individual model components: absorbed power-law (cyan), low-temperature (blue), and high-temperature blackbody (magenta). Bottom: corresponding residuals of the data compared to the best-fitting model.

differs from 2MASS J165315+2349 is that both the emission and absorption have comparable width and the emission (as well as the absorption) seems to be originating from ionised material. Such features are highly reminiscent of the well-established P Cygni-like profile detected in PDS 456 (Nardini et al. 2015), where the emission component arises from photons scattered back into our line of sight from the same outflowing ionised outflow, averaged over all the viewing angles. The complete set of blind-search line contours of all the remaining observations in the sample are plotted in Fig. E.1. The visual inspection of the residuals makes the Fe K emission/absorption profiles detections largely qualitative at this stage. Nonetheless, we now have a strong basis to carry out a systematic identification of iron K absorption features that might be arising from a UFO.

4.3. Modelling the Fe K band

In this paper, we only adopt phenomenological models that are homogeneously fitted across the whole sample. All the Fe K emission and absorption residuals arising from the line blind-search (see Fig. E.1) are fitted with a cosmologically redshifted Gaussian model (zgauss in XSPEC) added to Eqs. (1) and/or (2). Modelling the Fe K features this way allows us to characterise the significance and intrinsic properties of the lines, namely the centroid rest energy, the line width, and the overall strength with respect to the underlying continuum. In some cases, when the feature is broader, we fix their line widths (for simplicity) between $\sigma_{\text{width}} = 10$ eV–400 eV (depending on which produces a larger improvement to the fit). When the lines are broad/resolved, the line width is left as a free parameter (see Table 2). A strong emission profile corresponding to the neutral Fe Kα core at ~6.4 keV is present in almost every target. In some observations, of PG 0953+414,
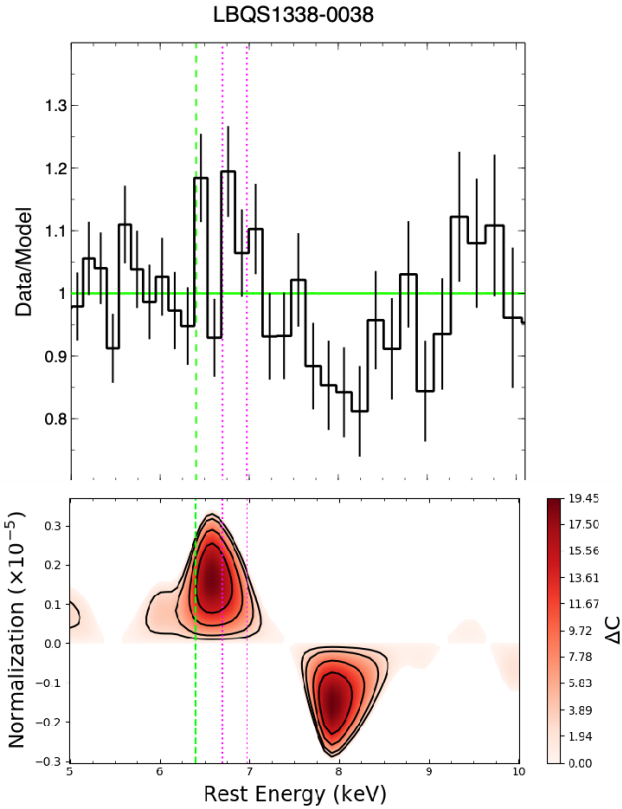
LBQS1338-0038

Fig. 4. Plot of the residuals and the corresponding closed confidence contours plot from the blind scan of the type 1 AGN LBQS 1338−0038. Top: data/model ratio plot for the EPIC-pn spectrum (MOS 1 and MOS 2 are not included for clarity), showing the residuals in the 5–10 keV band. A broad emission and absorption profiles are seen at ~6.6 keV and ~8 keV, respectively, suggesting a P Cygni-like profile. The vertical lines indicate the Fe Kα laboratory transition at E_{lab} = 6.40 keV (lime green) and Fe XXV and Fe XXVI at E_{lab} = 6.70 keV and 6.97 keV, respectively (magenta). The outer to inner closed contours correspond to a ΔC significance of (−2.3 = 68%), (−4.61 = 90%), (−9.21 = 99%), and (−13.82 = 99.9%) relative to the best-fitting continuum. Bottom: corresponding blind-search contours, showing the evidence of strong emission profiles at high confidence level (see the colour bar on the right).

PG 1425+267, PG 1626+554, PG 1352+183, PG 1216+069, PG 0947+396_obs1, 2MASS J105144+3539 and PG 0804+761, the Fe K emission lines are more complex (see Fig. E.1). Their Fe K emissions are broader and the centroid energies correspond to highly ionised iron emission in the Fe XXV and Fe XXVI domain. In the context of UFOs, broader iron K emission can arise from scattered photons from outflowing ionised material and can have crucial implications in determining the covering fraction of the outflowing gas (Sim et al. 2008, 2010; Nardini et al. 2015; Matzeu et al. 2016; Reeves & Braito 2019).

For the absorption features we estimated the outflow velocity by assuming that iron K absorption observed at energy E_{abs} is associated with H-like iron (Fe XXVI Lyα) gas, with laboratory rest-frame energy of E_0 = 6.97 keV. Assuming E_0 = 6.7 keV (i.e. Fe XXV Heα) would correspond in the above calculations to a faster v_{out}, given the larger degree of blueshift. Our choice of E_0 can be considered as a conservative choice for the outflow velocity estimate, based on the reference energy assumed. For a more appropriate identification of line transitions (i.e.

Fe XXV Heα, Fe XXVI Lyα, or Fe K-shell edges), we need to carry out a photoionisation modelling of the Fe K features (with XABS and XSTAR models), which can yield an accurate description of the physical conditions of the gas, for example its ionisation state. A comprehensive physically motivated analysis of the emission/absorption profiles of the entire sample is the subject of a forthcoming companion paper.

For quantifying the statistical significance of the Gaussian lines in our modelling, we first adopt the ΔC improvement as used for our blind-search method. More specifically, we compute the P_F significance derived by first obtaining the $\Delta C/\Delta \nu$ between the best fit with and without a specific Gaussian line and subsequently compute the F-test probability. We detected blueshifted Fe K absorption lines in 11 out of 22 sources at $P_F \gtrsim 95\%$, where 9/22 have $P_F \gtrsim 99\%$.

Numerous authors in the literature (e.g. Vaughan et al. 2003; Porquet et al. 2004b; Markowitz et al. 2006; T10; G13; Igo20, Parker et al. 2020) have established that to obtain an adequate statistical test when determining the significance of a detection of atomic lines in rather complex spectra, an extensive $\mathcal{MC}$ approach is required. In an absorption-line search framework we might detect unexpected lines at a specific energy, without any prior justification, (e.g. Protassov et al. 2002) over an arbitrary energy range. Indeed, as discussed in the next section, we find that our P_F improvements over-predict the detection probabilities, as opposed to a more robust $\mathcal{MC}$ simulation approach.

4.4. Monte Carlo approach

The $\mathcal{MC}$ simulation method has now been extensively adopted in the literature (e.g. Porquet et al. 2004b; Miniutti & Fabian 2006; Tombesi et al. 2010; Gofford et al. 2013; Nardini et al. 2019; Parker et al. 2020; Middei et al. 2020) in order to achieve a robust determination of the significance of a spectral line independently from the spectral noise and the quality of the detector. The $\mathcal{MC}$ approach overcomes the limitations of the often used F-test, which can sometimes over-predict the statistical significance of the line detection when compared to extensive $\mathcal{MC}$ simulations. In this paper the $\mathcal{MC}$ approach is focused on the Fe K absorption lines detected in 11 sources on the basis of $P_F \gtrsim 95\%$. We report the results on the detection probability based on $\mathcal{MC}$ in Table 2.

This process was carried out by following these steps. (i) The continuum baseline null-hypothesis model ($\mathcal{NHM}$) is our final best-fitting 0.3–10 keV model (see Table D.1) re-adjusted after removing the Gaussian absorption component. For each test, we simulated 1000 EPIC-pn, 1000 EPIC-MOS 1 and 1000 EPIC-MOS 2 source and background spectra, by using the fakeit command in XSPEC. The simulated spectra were generated with the same exposure times and response files from the original data and grouped accordingly. We adopt the $\mathcal{KB}$ binning (as described in Appendix C) with FTGROUPPHA. (ii) Our 0.3–10 keV simulated spectra are then fitted with the $\mathcal{NHM}$, which takes into account the associated uncertainties from the $\mathcal{NHM}$ itself. During this procedure, we fixed the line width of any broad Gaussian emission features present in the spectra (both in the soft and hard X-ray band) at their corresponding best-fit energy values from the real data and we let their intensities free to vary. The dual blackbody temperature, normalisations and any Galactic, intrinsic neutral/warm absorptions were frozen to their best-fit values of the real data reported in Table D.1. (iii) A narrow Gaussian profile, with line width fixed at zero, was then added to the $\mathcal{NHM}$, with normalisation also set to zero,

but free to fluctuate between negative and positive values, in order to probe both absorption and emission features. The rest-energy centroid of the Gaussian line was stepped between 5 and 10 kev in $\Delta E = 25$ eV increments with the STEPPAR command in XSPEC. Additionally, to prevent a local minimum during fitting, we also used the SHAKEFIT procedure developed by Simon Vaughan (see Sect. 3.2.2 in Hurkett et al. 2008). This process maps the ΔC variations relative to C_{null}, which are recorded after each step as $|\Delta C_{\text{noise}}|$. The degrees of freedom corresponding to both models are also recorded. (iv) The above steps were repeated through $S = 1000$ iterations for each test, which produced a $|\Delta C_{\text{noise}}|$ distribution under the null-hypothesis by mapping the statistical significance of any deviations from $\mathcal{NHM}$ due to random photon noise in the spectra. (v) The initial significance of the line derived from the real data $|\Delta C_{\text{line}}|$ was compared to the $|\Delta C_{\text{noise}}|$ distribution so that the number N of simulated spectra with a random noise fluctuation larger than the observed one can be evaluated. In case when the N simulated spectra have $|\Delta C_{\text{noise}}| \geq |\Delta C_{\text{line}}|$, the $\mathcal{MC}$ statistical significance ($P_{\mathcal{MC}}$) of the absorption line detection can be calculated as $P_{\mathcal{MC}} = 1 - \left(\frac{N}{S}\right)$ and reported in Table 2.

In order to compare with literature results, and following, for example, T10, we consider as robust detections only absorption lines with $P_{\text{F}} \gtrsim 99\%$ and $P_{\mathcal{MC}} \gtrsim 95\%$. The discussion of the Fe K emission/absorption detection rate in our sample is presented in Sect. 5.1.

5. Results

A total of 14 absorption features with energies $E_{\text{rest}} \gtrsim 7.1$ keV and $P_{\text{F}} \gtrsim 99\%$ are found. Of these, eight are robustly detected with $P_{\mathcal{MC}} \gtrsim 95\%$ while 6 have $P_{\mathcal{MC}} < 95\%$ and are therefore considered non-detections. In PG 1114+445 (ObsID 0651330501) an absorption line at $E_{\text{rest}} = 7.04^{+0.12}_{-0.08}$ keV was detected at the $P_{\text{F}} > 99\%$ confidence level. However, such a feature is likely consistent with a neutral iron K edge so no $\mathcal{MC}$ test was applied here.

In Fig. 5 (top), we plot the unfolded EPIC-pn, MOS 1, and 2 data showing the 8 Fe K absorption lines detections with $P_{\mathcal{MC}} \gtrsim 95\%$. To avoid model and data convolution issues, the spectra in each panel are initially unfolded against a simple $\Gamma = 2$ power law (with normalisation of 1) and subsequently their corresponding best-fitting model are superimposed. In Fig. 5 (middle) the plot is in terms of the EPIC data counts normalised by the effective areas and Fig. 5 (bottom) are their corresponding residuals.

We conservatively identify these Fe K absorption lines as highly ionised iron, specifically Fe XXVI Lyα K-shell transitions, all blueshifted with respect to their laboratory rest energies. Some of these lines can be a blend of both Fe XXV Heα and Fe XXVI Lyα resonant transitions and might be indistinguishable with the current EPIC energy resolution. In a forthcoming paper (Matzeu et al., in prep.), we will carry out a comprehensive physical modelling of these features where an accurate measurement of the ionisation balance, as well as density and velocity, of the outflowing gas can be achieved. A photoionisation analysis of the Fe K lines will also help in obtaining a quantitative identification of the absorption and emission features. As presented in Sect. 4.3, the corresponding outflow velocities were conservatively estimated by choosing $E_{\text{rest}} = 6.97$ keV as a reference energy (see Table 2).

5.1. Line detection rate

Here, we quantify the probability of whether or not the detected absorption lines are caused by statistical fluctuation ('shot noise'). This can be done by using the binomial distribution (e.g. T10; G13). For an event with a null probability, p, the likelihood of n detections after N trials is given by the expression

$$P(n; N, p) = \frac{N!}{n!(N-n)!} p^n (1-p)^{N-n}. \tag{3}$$

In this context, n is the number of absorption lines detected in N systems, and, depending on the latter quantity, we investigate two different cases where we take into account: case (i) all the individual targets, or $N_{\text{(i)}} = 22$; and case (ii) all the individual observations (with total net counts of ≥ 1500 cts in the 4–10 keV band), or $N_{\text{(ii)}} = 41$.

In case (i) we have $n_{95} = 7$ Fe K absorption line systems detected in $N_{\text{(i)}} = 22$ observations at a significance of $P_{\mathcal{MC}} \geq 95\%$. So the probability of one of these absorption profiles being due to fluctuating noise can be taken as $p < 0.05$. The probability of all of the observed absorption systems being associated with noise is then reasonably low, with $P_{95,\text{(ii)}} < 6.17 \times 10^{-5}$ ($\lesssim 0.006\%$). This suggests that the observed lines are unlikely to be associated with simple statistical fluctuations in the spectra.

In case (ii) we have a total of $n_{95} = 8$ detections out of $N_{\text{(ii)}} = 41$ individual observations. Here we have $P_{95,\text{(ii)}} < 6.89 \times 10^{-4}$ ($\lesssim 0.07\%$).

5.2. Photoionisation modelling of Fe K features: Initial results

Although this paper is solely focused on UFO detection, we present a preliminary photoionisation analysis of the Fe K features and we provide first-order physical measurements of their properties. This analysis is carried out so that our SUBWAYS results can be compared with those previously obtained in Tombesi et al. (2011, T11 hereafter) T11, G13 and Igo20. The search for absorption features and the Gaussian modelling of the absorption profiles in the Fe K band described in Sect. 4.3 suggest they can be ascribed to outflowing and highly ionised material likely associated with Fe XXV Heα–Fe XXVI Lyα transitions.

In contrast with the phenomenological models used before, modelling the absorption features with XSTAR allows us to probe the physical properties of the absorbing medium. More specifically, we are able to quantify the ionisation state (ξ), the column density (N_{H}) and the systemic redshift of the material relative to the observed one, which translates into the outflow velocity (v_{out}; see below for more details). Through the photoionisation modelling approach it is also possible to infer the geometric properties, such as the radial distance from the ionising source, the covering factor and the resulting overall kinematics (e.g. Gofford et al. 2015; Matzeu et al. 2017).

We replaced the Gaussian absorption profiles, detected at the $P_{\mathcal{MC}} \gtrsim 95\%$ confidence level, with XSTAR photoionisation models, generated with a power-law SED input spectrum of $\Gamma = 2$, by using the XSTAR suite v2.54a (Bautista & Kallman 2001; Kallman et al. 2004). We adopted various XSTAR grids with different turbulent velocity, defined as $\sigma_{\text{turb}} = \sqrt{2}\sigma$, so that an accurate description of the width of the Fe K absorption lines could be provided. Choosing a grid with a smaller σ_{turb} results in a smaller equivalent width of the profile in the data, and the absorption would saturate too quickly at lower N_{H}. So for each source we adopted grids with σ_{turb} ranging between 1000–10 000 km s^{-1} (see Table 3).

Table 2. Gaussian emission and absorption parameters in the Fe K band corresponding to a total of 41 observations.

Source (1)	XMM (2) ObsID	E_{em} (3) (keV)	σ_{width} (4) (eV)	Int (5) (10^{-6})	EW (6) (eV)	$\Delta C/\Delta\nu(P_F)$ (7)	E_{abs} (8) (keV)	σ_{width} (9) (eV)	Int (10) (10^{-6})	EW (11) (eV)	v_{Gau} (12) (c)	$\Delta C/\Delta\nu(P_F)$ (13)	P_{MC} (14)
PG 0052+251	0841480101	$6.40^{+0.06}_{-0.06}$	$10^{(f)}$	$3.3^{-1.5}_{+1.5}$	33^{-15}_{+15}	16.3/2 (>99.9%)							
PG 0953+414	0841480201	$6.42^{+0.06}_{-0.06}$	$10^{(f)}$	$1.9^{+1.0}_{-1.0}$	36^{+20}_{-20}	11.95/2 (99.75%)	$7.82^{+0.10}_{-0.10}$	$10^{(f)}$	$-1.5^{+0.9}_{-0.8}$	-43^{+24}_{-24}	$-0.116^{+0.012}_{-0.012}$	8.56/2 (98.62%)	82.1%
		$6.92^{+0.07}_{-0.08}$	100^{t}	$3.2^{+1.1}_{-1.0}$	73^{+26}_{-23}	24.87/2 (>99.99%)							
PG 1626+554	0841480401	$6.40^{+0.08}_{-0.07}$	$100^{(f)}$	$2.6^{+0.9}_{-0.9}$	63^{+22}_{-22}	21.02/2 (>99.99%)							
		$7.01^{+0.12}_{-0.15}$	$100^{(f)}$	$2.1^{+1.1}_{-1.1}$	60^{+36}_{-36}	9.87/2 (99.28%)							
PG 1202+281	0841480501	$6.45^{+0.05}_{-0.05}$	$10^{(f)}$	$2.1^{+1.0}_{-1.0}$	37^{+18}_{-18}	13.7/2 (99.89%)	$7.78^{+0.06}_{-0.06}$	$10^{(f)}$	$-1.9^{+0.9}_{-0.9}$	-45^{+21}_{-21}	$-0.113^{+0.012}_{-0.012}$	10.3/2 (99.42%)	**95.0%**
		$7.09^{+0.09}_{-0.08}$	$10^{(f)}$	$1.67^{+1.0}_{-1.0}$	34^{+21}_{+21}	8.0/2 (98.17%)							
PG 1435−067	0841480601	$6.37^{+0.06}_{-0.06}$	$10^{(f)}$	$1.8^{+0.78}_{-0.74}$	100^{+39}_{-36}	19.0/2 (>99.99%)	$8.28^{+0.70}_{-0.45}$	$400^{(f)}$	$-2.2^{+1.4}_{-1.4}$	-184^{+117}_{-117}	$-0.166^{+0.079}_{-0.053}$	9.52/2 (99.14%)	90.9%
SDSS J144414+0633	0841480701	$6.43^{+0.03}_{-0.03}$	$10^{(f)}$	$2.8^{+0.8}_{-0.8}$	64^{+18}_{-18}	37.48/2 (>99.99%)							
2MASS J165315+2349 [(†)]	0841480801	$6.37^{+0.03}_{-0.03}$	$10^{(f)}$	$3.4^{+0.9}_{-0.9}$	73^{+20}_{-20}	49.09/2 (>99.99%)	$7.42^{+0.06}_{-0.06}$	$10^{(f)}$	$-1.8^{+0.8}_{-0.8}$	-48^{+21}_{-21}	$-0.082^{+0.012}_{-0.012}$	14.39/2 (>99.9%)	> 99.9% [(‡)]
							$7.77^{+0.06}_{-0.07}$	$10^{(f)}$	$-1.8^{+0.9}_{-0.8}$	-56^{+28}_{-25}	$-0.108^{+0.009}_{-0.010}$	14.97/2 (>99.9%)	
		$8.87^{+0.13}_{-0.17}$	$100^{(f)}$	$2.5^{+1.3}_{-1.3}$	87^{+43}_{-39}	10.48/2 (99.64%)							
PG 1216+069	0841480901	$6.47^{+0.12}_{-0.13}$	182^{+181}_{-129}	$2.8^{+1.5}_{-1.2}$	68^{+36}_{-29}	21.28/3 (>99.99%)							
PG 0947+396 (Obs 1)	0841481001	$6.43^{+0.06}_{-0.06}$	$10^{(f)}$	$2.2^{+1.0}_{-1.0}$	88^{+31}_{-31}	23.8/2 (>99.99%)	$9.51^{+0.10}_{-0.11}$	10^{f}	$-2.2^{+1.0}_{-0.9}$	-169^{+77}_{-69}	$-0.300^{+0.010}_{-0.010}$	11.65/2 (99.7%)	**96.9%**
		$6.96^{+0.12}_{-0.11}$	$10^{(f)}$	$1.4^{+1.0}_{-0.9}$	64^{+45}_{-45}	9.47/2 (99.12%)							
PG 0947+396 (Obs 2)	0841482301	$6.35^{+0.06}_{-0.06}$	$100^{(f)}$	$3.0^{+0.9}_{-0.9}$	132^{+40}_{-40}	35.02/2 (>99.99%)							
WISE J053756−0245	0841481101	$6.40^{+0.06}_{-0.06}$	$10^{(f)}$	$1.5^{+0.6}_{-0.6}$	81^{+32}_{-32}	21.0/2 (99.99%)							
HB 891529+050	0841481301	$6.47^{+0.04}_{-0.04}$	$10^{(f)}$	$2.0^{+0.5}_{-0.5}$	103^{+26}_{-26}	38.88/2 (>99.99%)							
PG 1307+085	0841481401	$6.35^{+0.06}_{-0.06}$	$100^{(f)}$	$3.5^{+1.0}_{-1.0}$	64^{+18}_{-18}	35.74/2 (>99.99%)							
PG 1425+267	0841481501	$6.40^{+0.03}_{-0.03}$	$10^{(f)}$	$3.0^{+0.7}_{-0.7}$	73^{+17}_{-17}	48.12/2 (>99.99%)	$8.24^{+0.06}_{-0.06}$	10^{f}	$-1.2^{+0.6}_{-0.6}$	-46^{+23}_{-24}	$-0.166^{+0.009}_{-0.009}$	10.09/2 (99.36%)	93.2%
		$6.88^{+0.06}_{-0.06}$	$10^{(f)}$	$1.4^{+0.7}_{-0.7}$	38^{+20}_{-20}	11.91/2 (98.74%)							
PG 1352+183	0841481601	$6.53^{+0.13}_{-0.12}$	468^{+138}_{-113}	$6.0^{+1.8}_{-1.6}$	319^{+96}_{-85}	74.69/3 (>99.99%)							
2MASS J105144+3539	0841481701	$6.37^{+0.08}_{-0.08}$	$100^{(f)}$	$1.7^{+0.5}_{-0.5}$	156^{+75}_{-56}	35.66/3 (>99.99%)	$8.51^{+0.08}_{-0.07}$	100^{f}	$-0.78^{+0.38}_{-0.33}$	-108^{+52}_{-46}	$-0.197^{+0.009}_{-0.009}$	10.56/2 (99.49%)	**95.9%**
2MASS J0220−0728	0841481901	$6.39^{+0.05}_{-0.05}$	$10^{(f)}$	$1.3^{+0.5}_{-0.5}$	60^{+23}_{-23}	15.58/2 (>99.9%)							
LBQS 1338−0038	0841482101	$6.62^{+0.94}_{-0.21}$	311^{+432}_{-124}	$2.5^{+1.1}_{-1.3}$	$67^{+/}_{-35}$	15.09/2 (99.99%)	$8.03^{+0.20}_{-1.06}$	$378^{(\star)}$	$-3.6^{+1.1}_{-1.1}$	-130^{+41}_{-41}	$-0.139^{+0.02}_{-0.02}$	24.13/3 (>99.9%)	> 99.9%
							$11.06^{+0.29}_{-0.29}$	$378^{(f)}$	$-3.01^{+1.3}_{-1.3}$	-187^{+81}_{-81}	$-0.432^{+0.041}_{-0.041}$	10.00/2 (99.33%)	87.2%
PG 0804+761	0102040401	$6.33^{+0.08}_{-0.07}$	$10^{(f)}$	$8.2^{+5.4}_{-5.1}$	60^{+40}_{-37}	7.43/2 (97.56%)	$7.93^{+0.06}_{-0.06}$	10^{f}	$-11.7^{+4.6}_{-4.2}$	-133^{+52}_{-48}	$-0.128^{+0.007}_{-0.006}$	15.99/2 (>99.99%)	**99.8%**
		$6.96^{+0.16}_{-0.16}$	$10^{(f)}$	$8.4^{+5.7}_{-5.3}$	74^{+50}_{+47}	7.50/2 (97.65%)							
	0605110101	$6.41^{+0.08}_{-0.07}$	$100^{(f)}$	$8.0^{+2.8}_{-2.8}$	69^{+24}_{-24}	25.77/2 (>99.99%)							
		$6.81^{+0.16}_{-0.17}$	$10^{(f)}$	$4.7^{+2.3}_{-2.2}$	44^{+22}_{+21}	13.89/2 (>99.99%)							
	0605110201	$6.58^{+0.09}_{-0.09}$	388^{+104}_{-80}	$26.4^{+6.5}_{-5.7}$	328^{+81}_{-71}	115.0/3 (>99.99%)							
PG 1416−129	0203770201	$6.36^{+0.04}_{-0.05}$	$10^{(f)}$	$3.0^{+1.1}_{-1.1}$	61^{+22}_{-22}	22.13/2 (>99.99%)							
PG 1402+261	0400200101	$6.37^{+0.07}_{-0.07}$	$10^{(f)}$	$1.9^{+1.0}_{-1.0}$	82^{+55}_{-49}	10.88/2 (99.57%)							
		$7.40^{+0.09}_{-0.10}$	$10^{(f)}$	$1.5^{+1.0}_{-0.9}$	76^{+40}_{-40}	7.42/2 (97.55%)							
	0830470101	$6.15^{+0.15}_{-0.16}$	$100^{(f)}$	$1.1^{+0.7}_{-0.7}$	42^{+27}_{-27}	11.69/2 (99.71%)							
		$8.36^{+0.06}_{-0.06}$	$10^{(f)}$	$0.86^{+0.74}_{-0.72}$	67^{+58}_{-56}	7.74/2 (97.91%)							
HB89 1257+286	0204040101	$6.34^{+0.04}_{-0.04}$	100^{f}	$2.2^{+0.6}_{-0.5}$	85^{+23}_{-23}	38.3/2 (>99.99%)	$8.78^{+0.15}_{-0.16}$	$10^{(f)}$	$-1.1^{+0.7}_{-0.7}$	-81^{+54}_{-54}	$-0.227^{+0.016}_{-0.018}$	6.33/2 (95.78%)	65.8%
	0204040201	$6.37^{+0.04}_{-0.04}$	$10^{(f)}$	$1.5^{+0.5}_{-0.5}$	93^{+31}_{-31}	27.2/2 (>99.99%)							
	0204040301	$6.35^{+0.09}_{-0.08}$	$100^{(f)}$	$1.7^{+0.7}_{-0.7}$	82^{+34}_{-34}	18.9/2 (>99.99%)							
		$6.93^{+0.09}_{-0.09}$	$100^{(f)}$	$1.5^{+0.7}_{-0.7}$	84^{+38}_{-38}	14.5/2 (98.74%)							
	0304320201	$6.46^{+0.15}_{-0.13}$	284^{+213}_{-200}	$4.7^{+1.8}_{-1.5}$	156^{+60}_{-50}	27.2/3 (>99.99%)							
	0304320301	$6.49^{+0.08}_{-0.08}$	$10^{(f)}$	$1.2^{+0.7}_{-0.7}$	66^{+39}_{-39}	9.7/2 (99.23%)							
	0304320801	$6.41^{+0.13}_{-0.13}$	$10^{(f)}$	$1.1^{+0.8}_{-0.8}$	44^{+32}_{-32}	6.36/2 (95.84%)							
PG 1114+445	0109080801	$6.56^{+0.07}_{-0.07}$	200^{+57}_{-47}	$11.2^{+2.3}_{-2.2}$	279^{+57}_{-55}	103.9/2 (>99.99%)							
	0651330101	$6.48^{+0.06}_{-0.06}$	143^{+74}_{-56}	$8.3^{+2.4}_{-2.2}$	230^{+67}_{-61}	54.9/2 (>99.99%)	$7.49^{+0.29}_{-0.28}$	$300^{(f)}$	$-4.2^{+2.0}_{-1.9}$	-158^{+75}_{-71}	$-0.072^{+0.042}_{-0.042}$	11.71/2 (99.7%)	**95.5%**
	0651330301	$6.42^{+0.05}_{-0.05}$	$50^{(f)}$	$4.4^{+1.6}_{-1.4}$	133^{+43}_{-40}	29.2/2 (>99.99%)	$7.35^{+0.12}_{-0.19}$	$100^{(f)}$	$-2.6^{+1.2}_{-1.1}$	-94^{+38}_{-35}	$-0.053^{+0.017}_{-0.027}$	11.9/2 (99.7%)	**97.2%**
	0651330401	$6.48^{+0.06}_{-0.07}$	170^{+75}_{-55}	$10.6^{+4.4}_{-3.2}$	261^{+108}_{-79}	56.9/3 (>99.99%)	$7.21^{+0.11}_{-0.14}$	$10^{(f)}$	$-2.1^{+1.4}_{-1.3}$	-68^{+45}_{-42}	$-0.034^{+0.020}_{-0.015}$	8.3/2 (98.4%)	90.5%
	0651330501	$6.42^{+0.05}_{-0.04}$	$10^{(f)}$	$6.9^{+2.1}_{-1.9}$	178^{+54}_{-49}	49.6/2 (>99.99%)	$7.04^{+0.12}_{-0.08}$	$10^{(f)}$	$-2.7^{+1.4}_{-1.3}$	-79^{+41}_{-38}	–	10.02/2 (99.33%)	(N/A)[(♦)]
	0651330601	$6.51^{+0.05}_{-0.09}$	$100^{(f)}$	$8.5^{+4.7}_{-4.2}$	121^{+67}_{-60}	32.3/2 (>99.99%)							
	0651330701	$6.49^{+0.04}_{-0.04}$	$50^{(f)}$	$6.6^{+2.6}_{-2.3}$	117^{+46}_{-41}	29.4/2 (>99.99%)							
	0651330801	$6.42^{+0.09}_{-0.09}$	$100^{(f)}$	$5.3^{+1.2}_{-2.1}$	126^{+29}_{-50}	21.6/2 (>99.99%)							
		$9.02^{+0.16}_{-0.17}$	227^{+177}_{-156}	$5.7^{+3.6}_{-3.0}$	266^{+168}_{-140}	12.9/3 (99.51%)							
	0651330901	$6.44^{+0.06}_{-0.07}$	$50^{(f)}$	$4.4^{+2.2}_{-1.7}$	96^{+46}_{-37}	21.5/2 (>99.99%)							
	0651331001	$6.50^{+0.05}_{-0.06}$	134^{+67}_{-64}	$8.6^{+2.8}_{-2.4}$	214^{+70}_{-60}	48.8/3 (>99.99%)							
	0651331101	$6.42^{+0.09}_{-0.09}$	$50^{(f)}$	$4.3^{+2.6}_{-2.0}$	92^{+66}_{-43}	13.1/2 (99.86%)							

Notes. (1) Source name; (2) observation ID; (3) measured Gaussian emission line energy in the rest frame; (4) emission line energy width. The absorption lines were fitted with widths ranging between σ_{width} 10 eV–400 eV; (5) emission line intensity in units of ph cm^{-2} s^{-1}; (6) equivalent width; (7) change in C-stat fit statistic, degrees of freedom and the corresponding significance (in per cent) when the emission line is removed from the best fit; (8)–(11) same as (3)–(6) but for the Gaussian absorption line; (12) corresponding outflow velocity inferred from the rest-frame energy of the absorption line with $E_{rest} = 6.97$ keV as a reference energy; (13) same as (7); (14) $\mathcal{MC}$ significance of the absorption line where the $\gtrsim 95\%$ values are highlighted in bold. [(†)]In this observation the absorption profile is likely arising from a blend of a Fe XXV–XXVI pair, which could be resolved by binning the spectra with `grpmin1` (see Appendix C). [(‡)]as the two absorption lines are consistent with a Fe XXV–XXVI pair, we inferred the null probability of both profiles simultaneously as a false detection by multiplying the probabilities of each line. [(⋆)]In this P Cygni-like profile the line width of the emission is tied to that of the absorption as $\sigma_{em} = (\sigma_{abs}/E_{abs}) \times E_{em}$. [(f)]denotes a fixed parameter during fitting. [(♦)] A $\mathcal{MC}$ test was not applied for this feature as it is likely associated with a neutral Fe K edge.
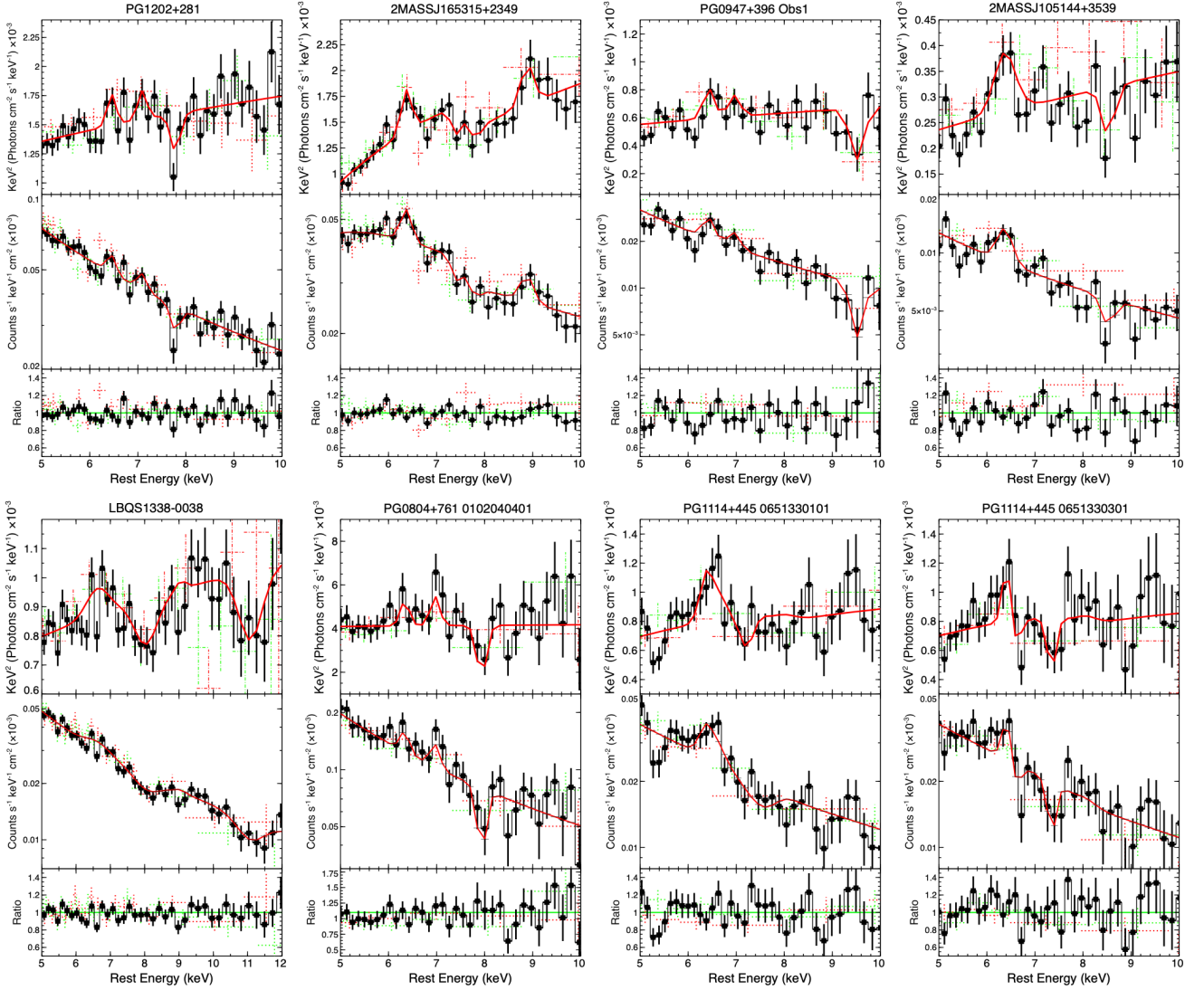
Fig. 5. *XMM-Newton* EPIC spectra and the corresponding best-fit models focused on the Fe K band. Top: unfolded EPIC-pn (black), EPIC-MOS 1 (dashed red), and EPIC-MOS 2 (dashed green) spectra, between 5–10 keV, of the eight observations where the Fe K absorption line was detected at $P_{MC} \gtrsim 95\%$. The spectra were firstly unfolded against a power law of $\Gamma = 2$, and their corresponding best-fitting model (solid red) was overlaid afterwards. Middle: corresponding EPIC data counts and best-fitting model. Bottom: data/model ratio. The presumed absorption features at ~9.2 keV and ~9.5 keV present in, for example, 2MASSJ105144+3539 and 2MASS J165315+2349, respectively, are simply not significant enough to be considered as detections (see Figs. 4 and E.1), and hence they were not included in the best-fitting models.

Table 3. XSTAR parameters for the Fe K absorption features detected in the SUBWAYS sample with $P_{MC} \gtrsim 95\%$.

				XSTAR parameters			
Source (1)	ObsID (2)	σ_{turb} (3) $(\mathrm{km\,s^{-1}})$	$\log(N_{\mathrm{H}})$ (4) $(\mathrm{cm^{-2}})$	$\log(\xi)$ (5) $(\mathrm{erg\,cm\,s^{-1}})$	v_{out} (6) (c)	$\Delta C/\Delta\nu$ (7)	(P_{F}) (8)
PG1202+281	0841480501	1000	>23.84	>5.02	$-0.108^{+0.010}_{-0.08}$	8.60/3	96.49%
2MASS J165315+2349[†]	0841480801	5000	$23.76^{+0.39}_{-0.15}$	$4.76^{+0.59}_{-0.42}$	$-0.110^{+0.008}_{-0.015}$	$-22.98/3$	>99.99%
PG0947+396 (Obs 1)	0841481001	5000	>23.68	$5.38^{+0.44}_{-1.27}$	$-0.305^{+0.037}_{-0.019}$	10.8/3	98.71%
2MASS J105144+3539	0841481701	1000	$22.78^{+0.67}_{-0.33}$	$4.10^{+0.35}_{-0.38}$	$-0.237^{+0.011}_{-0.010}$	10.9/3	98.77%
LBQS 1338−0038	0841482101	10000	$23.16^{+1.01}_{-0.22}$	$5.01^{+0.64}_{-0.38}$	$-0.152^{+0.020}_{-0.023}$	23.27/3	>99.99%
PG0804+761	0102040401	5000	$23.93^{+0.33}_{-0.27}$	>4.49	$-0.130^{+0.011}_{-0.011}$	11.1/3	98.88%
PG1114+445	0651330101	5000	$23.90^{+0.25}_{-0.16}$	$4.65^{+0.77}_{-0.44}$	$-0.072^{+0.017}_{-0.016}$	11.91/3	99.23%
	0651330301	5000	$23.61^{+0.10}_{-0.15}$	$3.56^{+0.10}_{-0.13}$	$-0.070^{+0.017}_{-0.015}$	62.08/3	>99.99%

Notes. (1) Source name; (2) observation ID; (3) intrinsic velocity broadening of the XSTAR grid; (4) column density and (5) gas ionisation state both in log scale; (6) change in C−stat fit statistic over degrees of freedoms when XSTAR is removed; (7) corresponding significance in per cent; (8) F-test probability significance.

The measured column densities are ranging between $10^{23} \lesssim N_{\rm H}/{\rm cm}^{-2} \lesssim 10^{24}$ with a mean value of $\log(\overline{N}_{\rm H}/{\rm cm}^{-2}) \sim 23.6$ and a median of $\log(\tilde{N}_{\rm H}/{\rm cm}^{-2}) \sim 23.8$. We also report the measured ionisation distribution, which is found to extend between $3.5 \lesssim \log(\xi/{\rm erg\,cm\,s}^{-1}) \lesssim 5.5$, with mean/median values of $\log(\overline{\xi}/{\rm erg\,cm\,s}^{-1}) \sim 4.7$ and $\log(\tilde{\xi}/{\rm erg\,cm\,s}^{-1}) \sim 4.8$, respectively.

The outflow velocity distribution measured with XSTAR[8] ranges between $-0.3 \lesssim v_{\rm out}/c \lesssim -0.1$ (see Table 3). The mean/median values are $\overline{v}_{\rm out} \sim -0.144\,c$ and $\tilde{v}_{\rm out} \sim -0.110\,c$, respectively. We also compare the outflow velocities measured with XSTAR and with the one measured from the Gaussian fitting. For the latter, the measured velocities are found to lie between $-0.3 \lesssim v_{\rm out}/c \lesssim -0.05$ (see Table 2) with mean/median values of $\overline{v}_{\rm out,Gauss} \sim -0.131\,c$ and $\tilde{v}_{\rm out,Gauss} \sim -0.113\,c$, respectively. We find that both the phenomenological and the physical modelling of the Fe K absorption features have the same distribution, as confirmed at the 99.7% confidence level by a Kologoromv-Smirnov test. The XSTAR-based approach returns a $\sim$10% higher mean velocity but a comparable median, within $\sim$3%.

In our sample a considerable fraction of the Fe K absorbers are characterised by material with high column density and highly ionised material, likely H-like iron. Such a result does not come as surprise when considering the hard average photon index ($\overline{\Gamma} \sim 1.8$) measured on the entire sample (see Fig. 6), which would over-ionise the outflowing material (see Matzeu et al. 2022, Figs. 2 and 3). A comprehensive photoionisation analysis with XSTAR (and other physically motivated wind models) will be presented in a companion paper, where customised photoionisation tables will be generated with more realistic optical/UV/X-ray SED inputs for each individual SUBWAYS source (e.g. Nardini et al. 2015; Matzeu et al. 2016).

6. Discussion

In this work we searched for Fe K absorption features in a sample of 22 targets (41 observations), of which 17 were observed as part of the *XMM-Newton* large programme carried out in AO18. Through a systematic blind line scan performed in all the observations and supported by a $\mathcal{MC}$ procedure, we detected iron K absorption lines in 7/22 sources (i.e. $\sim$30%) at the $P_{\mathcal{MC}} \gtrsim$ 95% confidence level. Through our statistical approach, we have found 2 robust Fe K absorption line detections at $P_{\mathcal{MC}} \gtrsim$ 99% in 2MASS J165315+2349 and LBQS 1338−0038. The remaining 5 detections are still significant but with $95\% \lesssim P_{\mathcal{MC}} \lesssim$ 99%, in PG 1202+281, 2MASS J105144+3539, PG 1114+445, PG 0804+761 and PG 0947+396 (see Table 2).

Such absorption (and sometimes emission) profiles are associated with highly ionised He- and/or H-like iron, arising from the outflowing material, as their centroid energy is blueshifted with respect to the QSO systemic redshift. In this paper we only focused on the search and phenomenological analysis of such features. Thus, for the estimate of the outflow velocities, we assumed FeXXVI Lyα at $E_{\rm rest} = 6.97$ keV as a reference energy for a conservative result, which corresponds to the lowest possible outflow velocity. Accordingly, we find that the average outflow velocity measured in our sample is $\overline{v}_{\rm out} = -0.133\,c$, as shown in Fig. 7.

For our search of Fe K absorption and emission features, an accurate parameterisation of the underlying broadband continuum (i.e. 0.3–10 keV) in each observation was required.
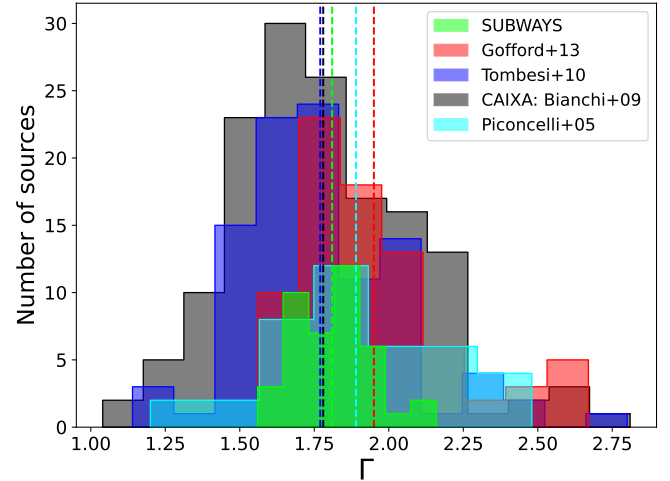

Fig. 6. Histogram comparing the photon index (Γ) measured in SUBWAYS (green; this work, with a mean value of $\overline{\Gamma} = 1.81$; vertical line) with those measured in an X-ray-selected sample (CAIXA sample, 150 sources with $\overline{\Gamma} = 1.78$; Bianchi et al. 2009), the PGQSO sample (Piconcelli et al. 2005, 40 sources $\overline{\Gamma} = 1.89$), and local AGNs (T10; G13 with $\overline{\Gamma} = 1.77$ and $\overline{\Gamma} = 1.95$, respectively).

We therefore summarise the phenomenological continuum findings of SUBWAYS. We found that 27 out of the 41 ($\sim$65%) SUBWAYS observations are characterised by intrinsic soft X-ray absorption. More specifically, 20/27 systems can be identified as fully covering, mildly ionised (warm) absorbers, while 5/27 are partially covering the line of sight. We note that 2/27 spectra are modified by a fully covering neutral absorber, where in 2MASS J165315+2349 the spectral curvature at energies <2 keV is caused by a column density $N_{\rm H} \sim 10^{23}$ cm^{-2}, consistent with the values measured in Seyfert 2 galaxies. We find that a prominent soft excess, at a >99% significance, is present in the vast majority of the spectra in our sample: 39/41; one zbbody component is required in 13/39 and two components in 26/39 sources.

In Fig. 6 we compare the primary continuum photon indices (Γ) with those measured in previous works in the literature: a purely X-ray-selected sample, CAIXA (Bianchi et al. 2009), an optically selected PGQSO sample (Piconcelli et al. 2005), and low-z AGNs analysed with *XMM-Newton* (T10) and *Suzaku* (G13). We find that the SUBWAYS sample tends to be characterised by $\Gamma < 2$ ($\overline{\Gamma} = 1.81$), only slightly harder compared to the optically selected PGQSO sample ($\overline{\Gamma} = 1.89$) and largely consistent with the CAIXA (Bianchi et al. 2009) ($\overline{\Gamma} = 1.78$) and T10 ($\overline{\Gamma} = 1.77$) samples. The mean photon index of the *Suzaku* sample is softer, with ($\overline{\Gamma} = 1.95$).

6.1. Sample comparisons

The SUBWAYS sample size is indeed small compared to those in T10; G13 and Igo20. With this in mind this selection of targets must be taken as an initial exploration of the intermediate-z population that is bridging the gap of UFOs studies between low- and high-z sources.

We find that our overall measurements seem to be skewed to higher values of $N_{\rm H}$ and $v_{\rm out}$ compared to (T10 and G13, whilst the ionisation state of the absorber is on the same order of magnitude (slightly lower). The latter parameter can be influenced by the SED input assumed when generating the photoionisation grids. We also find that the outflow velocity measured in PG 0947+396 (Obs1), being the highest in the sample, is
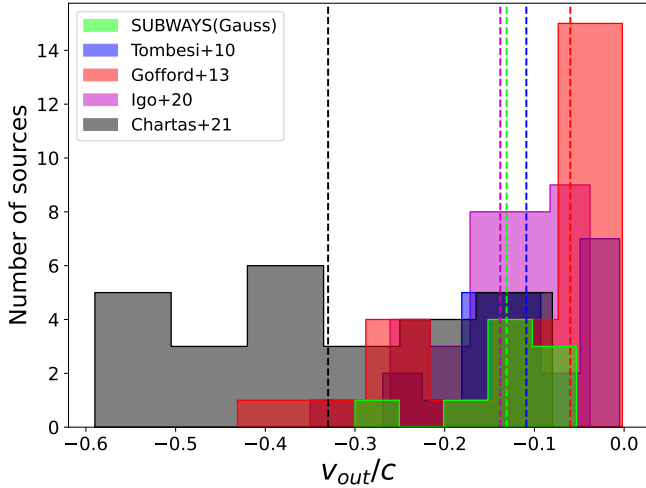
---

[8] The systemic redshift of the absorber obtained from fitting with XSTAR is given in the observer's rest-frame $z_{\rm abs}$ and related to $v_{z_{\rm abs}} = \left[(1+z_{\rm abs})^2 - 1\right]/\left[(1+z_{\rm abs})^2 + 1\right]$, and correcting for the systemic velocities of the sources u we obtain $v_{\rm out}/c = \left(u - v_{z_{\rm abs}}\right)/\left[1 - (uv_{z_{\rm abs}})\right]$.

Fig. 7. Distributions and mean outflow velocity values, indicated by the vertical dashed lines, as measured in: this work (SUBWAYS) $\bar{v}_{\text{out}} = -0.133c$; T10 $\bar{v}_{\text{out}} = -0.109c$; G13 $\bar{v}_{\text{out}} = -0.056c$; Igo20 $\bar{v}_{\text{out}} = -0.138c$; and C21 $\bar{v}_{\text{out}} = -0.330c$.

unlikely to be associated with outflowing, highly ionised material, but rather the result of an artefact of the EPIC CCD and/or some background issue. Although the absorption line is significantly detected at the $P_{\text{F}} > 99\%$ (Gaussian modelling) and $P_{\text{MC}} \sim 97\%$ ($\mathcal{MC}$ approach) confidence level, it is weakly detected with XSTAR at ~90%. Furthermore, an outflow velocity of $v_{\text{out}} > 0.30c$ is generally considered on the high end of the scale of ultra fast winds and can carry a huge amount of kinetic power (e.g. Matzeu et al. 2017; Reeves et al. 2018a). These events are more likely to be present in highly accreting sources where $L_{\text{bol}}/L_{\text{Edd}} \rightarrow 1$ (or above) and Eddington fractions of $L_{\text{bol}}/L_{\text{Edd}} \sim 10\%$ (Bianchi et al. 2009) might be not enough to drive such strong outflows, although it cannot be ruled out as magneto-hydrodynamic (MHD) driving mechanisms could come into play (e.g. Fukumura et al. 2010, 2022; Kraemer et al. 2018; Luminari et al. 2021), especially in low-Eddington regimes.

In Fig. 7, we show the v_{out} distributions, and their mean values, measured with *XMM-Newton* in previous works in the literature, such as in T10 $\bar{v}_{\text{out}} = -0.109\,c$; Igo20 $\bar{v}_{\text{out}} = -0.138\,c$; C21 $\bar{v}_{\text{out}} = -0.330\,c$. An interesting trend is shown in Fig. 7. By looking at all the measurements, the UFO outflow velocities seem to increase with redshift. Although the statistical footing of this trend is beyond the scope of this paper, we can recognise that such behaviour does arise from a high-L_{bol} selection bias expected in sources at progressively higher redshift as the feeding becomes stronger (e.g. Di Matteo et al. 2005), in particular due to the larger inflow of cold gas mass triggering chaotic cold accretion and boosting accretion rates by a few orders of magnitude compared with quiescent hot modes (e.g. Gaspari et al. 2017). Another way to interpret this trend is simply realise that the outflow velocity seems to increase with the luminosity (e.g. Saez & Chartas 2011; Matzeu et al. 2017; Chartas & Canas 2018, C21), as shown below in Fig. 8, and on the other hand the most luminous sources are observed at higher z. Additionally, another possible bias that is involved at higher z is that higher velocity shifts become more detectable with increasing redshift.

In Fig. 8 we show the wind velocities, as measured from our X-ray spectral fits with Gaussian lines and tabulated in Table 2, plotted against the bolometric luminosity of the SUBWAYS targets (see Table 1) shown as red stars. We added and recomputed the fit of the correlation of v_{wind} versus L_{bol} of the
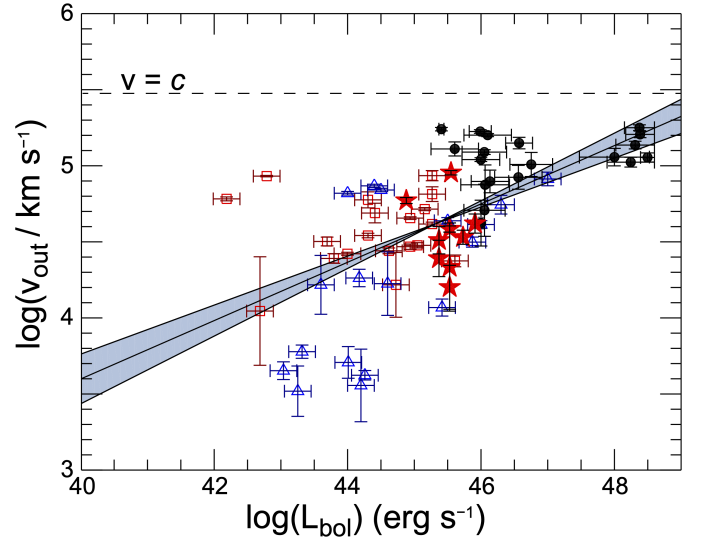

Fig. 8. Outflow velocity of the ionised absorber for our SUBWAYS targets (red filled stars) plotted against their bolometric luminosity. Also plotted are the same quantities as derived in the analysis of the low-z AGN samples of Tombesi et al. (2012, red empty squares) and G13 (blue empty triangles) and in the high-z AGN sample of C21 (black filled circles). The power-law least-squares fit to the combined samples (a total of 49 individual objects and 63 observations) is shown with a solid line. The shaded area represents the uncertainty of the slopes of our fits to the data. Here the outflow velocity is simply described as the absolute value of v_{out}.

low-z (T10; G13, red squares and blue triangles, respectively) and high-z samples already presented in C21, including also our SUBWAYS measurements. For all samples, bolometric luminosities are consistently computed from the 2–10 keV luminosities assuming a luminosity-dependent bolometric correction (Duras et al. 2020). The best fit parameters of a linear relation in log space of $\log(v_{\text{out}}) = A(L_{\text{bol}})^B$ are $A = -3.88 \pm 1.40$ and $B = 0.19 \pm 0.03$. Overall, the SUBWAYS data fit right between the low- and the high-z data. We find a Kendall's (rank) correlation coefficient of $\tau = 0.45$ with a null probability of $p_{\text{null}} = 1.8 \times 10^{-7}$. The strength and slope of this correlation is partially driven by the six data points in C21, with $\log(L_{\text{bol}}/ \text{erg s}^{-1}) \gtrsim 48$, that may be affected by additional uncertainties associated with the magnification factor due to lensing.

The low- and high-z fit correlation in C21 (see their Table 10) returned a slope of $B = 0.20 \pm 0.03$, a correlation coefficient of $\tau = 0.51$ with a null probability $p_{\text{null}} = 6.0 \times 10^{-8}$. Their slope is consistent with our measurement, whereas their coefficient is about 10% higher, which suggests that our correlation, with all the four samples included, is slightly weaker than in C21. A similar correlation was also observed by Matzeu et al. (2017) in the luminous QSO PDS 456 between the *XMM-Newton*, *NuSTAR*, and *Suzaku* observation from 2001–2014. The slope of the correlation in Matzeu et al. (2017, i.e. 0.22±0.04) is largely consistent with what we have found here.

Overall, with our result we can conclude that there is a correlation between the outflow velocities and bolometric luminosities within the overall low- intermediate- high-z samples. A positive correlation with a slope of 0.5 between outflow velocities and the luminosities of the AGNs is what it would be expected in a radiatively driven wind scenario as the radiation pressure plays a key role in driving the outflows.

The fact that the observed slope is lower than the expected value can be explained in several ways. One possible

explanation, already suggested in C21, is that we did not include outflows with velocities $\lesssim 10\,000\ \mathrm{km\,s^{-1}}$, as in T10.

Another plausible explanation is that, as the luminosity keep increasing, the inner part of the UFOs detected in SUBWAYS might be over-ionised, with weaker absorption features (e.g. Parker et al. 2017; Pinto et al. 2018) leading to their observability being pushed to the outer streamlines. Within this regime the observed velocities, due to their radial dependence, would appear slightly slower and such a physical condition leads to an overall flattening of the slope (Matzeu et al. 2017) from the nominal value of 0.5. The outflows shown in Fig. 8 have a range of mass outflow rates and black hole masses, so it is not clear that a simple scaling of velocity with luminosity is likely. If instead we assume that all the systems are close to their Eddington luminosities L_{Edd} and the outflows have the Eddington momenta L_{Edd}/c (see e.g. King 2003; King & Pounds 2015, and references therein) one finds that the velocities should be of order $0.1\,c$, as observed (see also Fig. 7).

In reality, the driving (and launching) mechanism responsible for the observed UFOs are likely the result of a complex interaction between radiation pressure and MHD driving. Indeed, it was previously found, in Matzeu et al. (2016) that in the powerful disc wind observed in PDS 456 in 2013, the radiation pressure alone, imparted from a strong flare, could have not deposit enough kinetic power on the outflowing material and hence suggesting that an additional launching mechanism, such as MHD, was also involved. Decoupling and assessment of each individual contribution remains a challenging subject in disc wind physics with the current CCD detectors.

6.2. Strong features around rest energies of 9 keV

In our SUBWAYS sample, the Fe K absorption line with the highest degree of blueshift was detected in PG 0947+396 (Obs1) at $E_{\mathrm{rest}} = 9.5 \pm 0.1\ \mathrm{keV}$ ($E_{\mathrm{obs}} \sim 7.9\ \mathrm{keV}$).

Despite its reasonable significance (see Table 2), there are a few caveats that could rule out its UFO identification. The energy shift from the H-like iron rest energy is rather large (even larger if He-like Fe is considered), and corresponds to an outflow velocity of $v_{\mathrm{out}} = -0.30 \pm 0.01c$, which is, by far, the fastest of the sample. Such a result could be (in principle) at odds considering the relatively low Eddington fraction of this source (i.e. $L_{\mathrm{bol}}/L_{\mathrm{Edd}} \sim 0.06$). These kinds of outflow velocities are more common in sources that are accreting near or above their Eddington limit, for example PDS 456. In this campaign, a second $\sim 60\,\mathrm{ks}$ observation (PG 0947+396 Obs2) was carried out about 5 months later and no Fe K absorption line was detected in the spectra (see Fig. E.1). The same applies for the first 20 ks XMM-Newton observation in 2001. Having said that, it is not impossible to have such a powerful UFO in a low-Eddington regime as other driving mechanisms, such as MHD, could play a key role (e.g. Fukumura et al. 2017). Indeed, further monitoring of this source will shed some light on the presence of a UFO.

Strong residuals in emission at $E_{\mathrm{rest}} \sim 9\ \mathrm{keV}$ are detected in 2MASS J165315+2349 and PG 1114+445 (0651330801) at the $P_{\mathrm{F}} > 99\%$ confidence level, which might be associated with a possible high-order iron K transition or perhaps associated with an instrumental calibration artefact. The origin of this feature could be associated with Ni XXVII Heβ $1s \rightarrow 3p$, or a blend thereof; however, no lower transitions are observed in the spectra. Such a feature is also observed in PG 1114+445, as blueshifted Fe XXVI Lyβ (8.25 keV). The dominant emission line in the pn background is the Cu Kα line at 8.04 keV. Weaker surrounding lines include Ni Kα (7.47 keV), Zn Kα (8.63 keV) and Cu Kβ (8.90 keV).

So another possible origin of these spurious features might arise from background subtraction issues during the data reduction process, or even from the detector itself such as in PG 1114+445. After a careful check we confirm that the line detections are genuine as no such issues were found. A thorough characterisation of the physical properties of the winds responsible for the detected Fe K lines will be carried out by using physically motivated models such as XSTAR, XABS, WINE (Luminari et al. 2021), and XRADE (Matzeu et al. 2022), and will be presented in a forthcoming SUBWAYS paper.

A second absorption line at $E_{\mathrm{rest}} \sim 11\ \mathrm{keV}$ ($E_{\mathrm{obs}} \sim 9\ \mathrm{keV}$) is detected in LBQS 1338−0038 at the $P_{\mathrm{F}} = 99.3\%$ confidence level however, following a $\mathcal{MC}$ procedure the significance of the line drops considerably to $P_{\mathcal{MC}} = 87.2\%$. This discrepancy in the detection can be likely attributed to the lack of data at energies $E_{\mathrm{obs}} > 10\ \mathrm{keV}$ being at the edge of the XMM-Newton band pass, and hence extra care is needed. Nonetheless, this high energy absorption feature is also present during a $\sim 50\,\mathrm{ks}$ NuSTAR exposure one year later in 2020 (PI Bianchi). A joint analysis focused on of the XMM-Newton and NuSTAR data of LBQS 1338−0038 will be presented in a companion letter (Matzeu et al., in prep.).

7. Summary and conclusions

We have carried out a systematic search focused on absorption features in the Fe K band in a sample of 22 (41 observations) luminous ($2 \times 10^{45} \lesssim L_{\mathrm{bol}}/\mathrm{erg\,s^{-1}} \lesssim 2 \times 10^{46}$) AGNs at intermediate redshifts ($0.1 \lesssim z \lesssim 0.4$) as part of the large XMM-Newton programme SUBWAYS. For each XMM-Newton observation, the data reduction was performed by optimising the level of background in order to increase of the S/N within the 4–10 keV band . Afterwards, an additional and crucial step was the appropriate choice of an optimal spectral binning to avoid a loss of information for any search of weak features, such as UFOs. We applied the four spectral binnings that are most used in the literature, and subsequently, after cross-checking them, all our results are based on the $\mathcal{KB}$ binning.

The main results are summarised below:

– We carried out an XMM-Newton broadband analysis between 0.3 and 10 keV. We find that in 27 out of 41 observations ($\sim 65\%$) our targets have intrinsic absorption in the soft X-rays, of which $\sim 70\%$ can be identified as fully covering, mildly ionised (warm) absorbers and 5 out of 27 ($\sim 30\%$) partially cover the line of sight.

– We then analysed the EPIC spectra of each of the 41 observations by first performing a series of blind-search line scans, in both emission and absorption, focused on the 5–10 keV band. For the overall Fe K emissions, the energies are in the range $6.2 \lesssim E_{\mathrm{rest}}/\mathrm{keV} \lesssim 9$, $\sim 90\%$ are consistent with the Fe Kα core (detected in 20 out of 22 targets), and $\sim 36\%$ are consistent with Fe XXV–XXVI (detected in 8 out of 22 targets). Their equivalent widths are in the range of $10 \lesssim EW/\mathrm{eV} \lesssim 468$, and the high-end values are due to complex emission features such as in PG 1352+183, likely arising from a blend between Fe K$\alpha[\beta]$ and Fe XXV.

– For the Fe K absorption features, we detected 14 absorption lines at the $P_{\mathrm{F}} \gtrsim 99\%$ confidence level with energies in the range $7 \lesssim E_{\mathrm{rest}}/\mathrm{keV} \lesssim 11$; $\sim 85\%$ are consistent with Fe XXV–XXVI, and one detection is consistent with an iron K edge. Their equivalent widths are in the range $-200 \lesssim EW/\mathrm{eV} \lesssim -40$, which is in line with what is expected for relatively narrow Fe K absorption profiles.

- Thanks to extensive $\mathcal{MC}$ simulations, we confirmed absorption lines corresponding to highly ionised iron in 7 out of 22 sources. These findings yield a UFO detection fraction of $\sim 30\%$ of the total sample, at a $P_{\mathcal{MC}} \gtrsim 95\%$ significance level. These features likely correspond to Fe XXV Heα and/or Fe XXVI Lyα. By using the Fe XXVI lab transition as the reference energy, we measured outflow velocities in the range $-0.3 \lesssim v_{\rm out}/c \lesssim -0.05$ with average and median velocities of $\bar{v}_{\rm out} = -0.133\,c$ and $\tilde{v}_{\rm out} = -0.110\,c$.

- In this work we also present preliminary results of photoionisation modelling of the iron K features detected at the $P_{\mathcal{MC}} \gtrsim 95\%$ confidence level with XSTAR. We find median values of $\log(\tilde{N}_{\rm H}/\,{\rm cm}^{-2}) \sim 23.8$ and $\log(\tilde{\xi}/{\rm erg\,cm\,s}^{-1}) \sim 4.8$ for the column densities and ionisation parameter, respectively.

- The measured outflow velocities with XSTAR are in the range $-0.3 \lesssim v_{\rm out}/c \lesssim -0.1$, where the mean and median values are $\bar{v}_{\rm out} \sim -0.144$ and $\tilde{v}_{\rm out} \sim -0.110$, respectively. Such a distribution is largely comparable with the outflow velocities measured with the phenomenological (Gaussian) modelling. Such results confirm that the absorption detected in the Fe K band arises from fast, highly ionised material with a high column density, as typically observed in UFOs.

- By comparing our results with previous work, we computed a power-law least-squares fit to the low-z (T10; G13), intermediate-z (SUBWAYS), and high-z (C21) data, which show a positive correlation between outflow velocity and bolometric luminosity within the overall low-, intermediate-, and high-z samples, with slope 0.19 ± 0.03. Such a $v_{\rm out}$–$L_{\rm bol}$ correlation is also observed in Matzeu et al. (2017) with a slope of 0.22 ± 0.04.

The outcome of this work independently provides further support for the existence of highly ionised matter propagating at mildly relativistic speeds, which is expected to play a key role in the self-regulated AGN feeding-feedback loop that shapes galaxies, as shown by hydrodynamical multi-phase simulations (Gaspari et al. 2020, for a review). These results suggest that the likely dominant driving mechanism of UFOs is radiation pressure arising in high-accretion regimes. It is important to note that MHD also plays a key role in the driving and launching mechanism of disc winds, and future observations at micro-calorimeter resolution will contribute towards distinguishing each component.

An alternative scenario that has been put forward is that the origin of Fe K absorption features can be attributed to a layer of hot gas located at the surface of the accretion disc rather than from an outflowing wind (Gallo et al. 2013). Thus, the prominent and blueshifted absorption lines are the result of a strong relativistic reflection component that dominates the hard X-ray continuum rather than the primary emission. This model was successfully applied to the NLSy1 IRAS13224−3809 by Fabian et al. (2020). The unprecedented spectral micro-calorimeter resolution from future UFO observations, such as X-Ray Imaging Spectroscopy Mission (*XRISM*/Resolve; Tashiro et al. 2020) and Advanced Telescope for High-ENergy Astrophysics/X-ray Integral Field Unit (*Athena*/X-IFU; Barret et al. 2018), will greatly contribute towards disentangling each of these scenarios, including the disc wind's launching and driving physical mechanism (e.g. Giustini & Proga 2012; Fukumura et al. 2022, Dadina et al., in prep., Matzeu et al., in prep.).

References

Aird, J., Coil, A. L., Georgakakis, A., et al. 2015, MNRAS, 451, 1892
Arnaud, K. A. 1996, ASP Conf. Ser., 101, 17
Ballantyne, D. R., & Xiang, X. 2020, MNRAS, 496, 4255
Barret, D., Lam Trong, T., den Herder, J.-W., et al. 2018, Proc. SPIE, 10699, 106991G
Bautista, M. A., & Kallman, T. R. 2001, ApJS, 134, 139
Bertola, E., Dadina, M., Cappi, M., et al. 2020, A&A, 638, A136
Bianchi, S., Guainazzi, M., Matt, G., Fonseca Bonilla, N., & Ponti, G. 2009, A&A, 495, 421
Bischetti, M., Maiolino, R., Carniani, S., et al. 2019a, A&A, 630, A59
Bischetti, M., Piconcelli, E., Feruglio, C., et al. 2019b, A&A, 628, A118
Blustin, A. J., Page, M. J., Fuerst, S. V., Branduardi-Raymont, G., & Ashton, C. E. 2005, A&A, 431, 111
Boller, T., Liu, T., Weber, P., et al. 2021, A&A, 647, A6
Braito, V., Reeves, J. N., Gofford, J., et al. 2014, ApJ, 795, 87
Braito, V., Reeves, J. N., Matzeu, G. A., et al. 2018, MNRAS, 479, 3592
Brusa, M., Bongiorno, A., Cresci, G., et al. 2015, MNRAS, 446, 2394
Brusa, M., Cresci, G., Daddi, E., et al. 2018, A&A, 612, A29
Cash, W. 1979, ApJ, 228, 939
Chartas, G., & Canas, M. H. 2018, ApJ, 867, 103
Chartas, G., Brandt, W. N., Gallagher, S. C., & Garmire, G. P. 2002, ApJ, 579, 169
Chartas, G., Charlton, J., Eracleous, M., et al. 2009, New A Rev, 53, 128
Chartas, G., Cappi, M., Vignali, C., et al. 2021, ApJ, 920, 24
Cicone, C., Maiolino, R., Sturm, E., et al. 2014, A&A, 562, A21
Cicone, C., Severgnini, P., Papadopoulos, P. P., et al. 2018, ApJ, 863, 143
Costa, T., Sijacki, D., & Haehnelt, M. G. 2014, MNRAS, 444, 2355
Crenshaw, D. M., Kraemer, S. B., & George, I. M. 2003, ARA&A, 41, 117
Cresci, G., Mainieri, V., Brusa, M., et al. 2015, ApJ, 799, 82
Dadina, M., Vignali, C., Cappi, M., et al. 2016, A&A, 592, A104
Dauser, T., García, J., Parker, M. L., Fabian, A. C., & Wilms, J. 2014, MNRAS, 444, L100
Di Matteo, T., Springel, V., & Hernquist, L. 2005, Nature, 433, 604
Done, C., Davis, S. W., Jin, C., Blaes, O., & Ward, M. 2012, MNRAS, 420, 1848
Duras, F., Bongiorno, A., Ricci, F., et al. 2020, A&A, 636, A73
Eckert, D., Gaspari, M., Gastaldello, F., Le Brun, A. M. C., & O'Sullivan, E. 2021, Universe, 7, 142
Fabian, A. C. 2012, ARA&A, 50, 455
Fabian, A. C., Reynolds, C. S., Jiang, J., et al. 2020, MNRAS, 493, 2518
Feruglio, C., Maiolino, R., Piconcelli, E., et al. 2010, A&A, 518, L155
Feruglio, C., Fiore, F., Carniani, S., et al. 2015, A&A, 583, A99
Feruglio, C., Ferrara, A., Bischetti, M., et al. 2017, A&A, 608, A30
Fiore, F., Feruglio, C., Shankar, F., et al. 2017, A&A, 601, A143
Fukumura, K., Kazanas, D., Contopoulos, I., & Behar, E. 2010, ApJ, 715, 636
Fukumura, K., Kazanas, D., Shrader, C., et al. 2017, Nat. Astron., 1, 0062
Fukumura, K., Dadina, M., Matzeu, G., et al. 2022, ApJ, 940, 6
Gabriel, C., Denby, M., Fyfe, D. J., et al. 2004, ASP Conf. Ser., 314, 159
Gallo, L. C., Fabian, A. C., Grupe, D., et al. 2013, MNRAS, 428, 1191
García, J., Dauser, T., Reynolds, C. S., et al. 2013, ApJ, 768, 146
García, J., Dauser, T., Lohfink, A., et al. 2014, ApJ, 782, 76
García, J. A., Kara, E., Walton, D., et al. 2019, ApJ, 871, 88
Gaskell, C. M. 1982, ApJ, 263, 79
Gaspari, M., & Sądowski, A. 2017, ApJ, 837, 149
Gaspari, M., Brighenti, F., & Ruszkowski, M. 2013, Astron. Nachr., 334, 394
Gaspari, M., Temi, P., & Brighenti, F. 2017, MNRAS, 466, 677
Gaspari, M., Eckert, D., Ettori, S., et al. 2019, ApJ, 884, 169
Gaspari, M., Tombesi, F., & Cappi, M. 2020, Nat. Astron., 4, 10
Giustini, M., & Proga, D. 2012, ApJ, 758, 70
Giustini, M., & Proga, D. 2019, A&A, 630, A94
Gofford, J., Reeves, J. N., Tombesi, F., et al. 2013, MNRAS, 430, 60
Gofford, J., Reeves, J. N., McLaughlin, D. E., et al. 2015, MNRAS, 451, 4169
Green, J. C., Froning, C. S., Osterman, S., et al. 2012, ApJ, 744, 60
Halpern, J. P. 1984, ApJ, 281, 90
Hamann, F., Chartas, G., Reeves, J., & Nardini, E. 2018, MNRAS, 476, 943
Harrison, C. M., Alexander, D. M., Mullaney, J. R., & Swinbank, A. M. 2014, MNRAS, 441, 3306

Heckman, T. M., & Best, P. N. 2014, ARA&A, 52, 589
HI4PI Collaboration (Ben Bekhti, N., et al.) 2016, A&A, 594, A116
Hurkett, C. P., Vaughan, S., Osborne, J. P., et al. 2008, ApJ, 679, 587
Igo, Z., Parker, M. L., Matzeu, G. A., et al. 2020, MNRAS, 493, 1088
Jansen, F., Lumb, D., Altieri, B., et al. 2001, A&A, 365, L1
Jiang, J., Fabian, A. C., Dauser, T., et al. 2019, MNRAS, 489, 3436
Kaastra, J. S., & Bleeker, J. A. M. 2016, A&A, 587, A151
Kaastra, J. S., Mewe, R., & Nieuwenhuijzen, H. 1996, in 11th Colloquium on UV and X-ray Spectroscopy of Astrophysical and Laboratory Plasmas, 411
Kaastra, J. S., Mewe, R., Liedahl, D. A., Komossa, S., & Brinkman, A. C. 2000, A&A, 354, L83
Kaastra, J. S., Kriss, G. A., Cappi, M., et al. 2014, Science, 345, 64
Kallman, T. R., Palmeri, P., Bautista, M. A., Mendoza, C., & Krolik, J. H. 2004, ApJS, 155, 675
Kaspi, S., Brandt, W. N., Netzer, H., et al. 2000a, ApJ, 535, L17
Kaspi, S., Smith, P. S., Netzer, H., et al. 2000b, ApJ, 533, 631
King, A. 2003, ApJ, 596, L27
King, A. 2005, ApJ, 635, L121
King, A., & Pounds, K. 2015, ARA&A, 53, 115
King, A. R., Zubovas, K., & Power, C. 2011, MNRAS, 415, L6
Kormendy, J., & Ho, L. C. 2013, ARA&A, 51, 511
Kraemer, S. B., Tombesi, F., & Bottorff, M. C. 2018, ApJ, 852, 35
Kriss, G. A., Lee, J. C., Danehkar, A., et al. 2018, ApJ, 853, 166
Kriss, G. A., Mehdipour, M., Kaastra, J. S., et al. 2019, A&A, 621, A12
Krongold, Y., Longinotti, A. L., Santos-Lleó, M., et al. 2021, ApJ, 917, 39
Laha, S., Guainazzi, M., Dewangan, G. C., Chakravorty, S., & Kembhavi, A. K. 2014, MNRAS, 441, 2613
Laha, S., Guainazzi, M., Chakravorty, S., Dewangan, G. C., & Kembhavi, A. K. 2016, MNRAS, 457, 3896
Laha, S., Reynolds, C. S., Reeves, J., et al. 2021, Nat. Astron., 5, 13
Lanzuisi, G., Giustini, M., Cappi, M., et al. 2012, A&A, 544, A2
Longinotti, A. L., Krongold, Y., Guainazzi, M., et al. 2015, ApJ, 813, L39
Longinotti, A. L., Vega, O., Krongold, Y., et al. 2018, ApJ, 867, L11
Luminari, A., Piconcelli, E., Tombesi, F., et al. 2018, A&A, 619, A149
Luminari, A., Nicastro, F., Elvis, M., et al. 2021, A&A, 646, A111
Maccagni, F. M., Serra, P., Gaspari, M., et al. 2021, A&A, 656, A45
Magorrian, J., Tremaine, S., Richstone, D., et al. 1998, AJ, 115, 2285
Maiolino, R., Gallerani, S., Neri, R., et al. 2012, MNRAS, 425, L66
Mallick, L., Fabian, A. C., García, J. A., et al. 2022, MNRAS, 513, 4361
Marasco, A., Cresci, G., Nardini, E., et al. 2020, A&A, 644, A15
Markowitz, A., Reeves, J. N., & Braito, V. 2006, ApJ, 646, 783
Mathur, S., Wilkes, B. J., & Aldcroft, T. 1997, ApJ, 478, 182
Mathur, S., Wilkes, B., & Elvis, M. 1998, ApJ, 503, L23
Matzeu, G. A., Reeves, J. N., Nardini, E., et al. 2016, MNRAS, 458, 1311
Matzeu, G. A., Reeves, J. N., Braito, V., et al. 2017, MNRAS, 472, L15
Matzeu, G. A., Lieu, M., Costa, M. T., et al. 2022, MNRAS, 515, 6172
McKernan, B., Yaqoob, T., & Reynolds, C. S. 2007, MNRAS, 379, 1359
McKinley, B., Tingay, S. J., Gaspari, M., et al. 2022, Nat. Astron., 6, 109
Mehdipour, M., Kriss, G. A., Krongold, Y., et al. 2022, ApJ, 930, 166
Mehdipour, M., Kriss, G. A., Brusa, M., et al. 2023, A&A, 670, A183
Middei, R., Bianchi, S., Cappi, M., et al. 2018, A&A, 615, A163
Middei, R., Tombesi, F., Vagnetti, F., et al. 2020, A&A, 635, A18
Miniutti, G., & Fabian, A. C. 2006, MNRAS, 366, 115
Mizumoto, M., Done, C., Tomaru, R., & Edwards, I. 2019, MNRAS, 489, 1152
Morganti, R., Tadhunter, C. N., & Oosterloo, T. A. 2005, A&A, 444, L9
Murphy, E. M., Lockman, F. J., Laor, A., & Elvis, M. 1996, ApJS, 105, 369
Murray, N., Chiang, J., Grossman, S. A., & Voit, G. M. 1995, ApJ, 451, 498
Murray, N., Quataert, E., & Thompson, T. A. 2005, ApJ, 618, 569
Nardini, E., & Zubovas, K. 2018, MNRAS, 478, 2274
Nardini, E., Fabian, A. C., Reis, R. C., & Walton, D. J. 2011, MNRAS, 410, 1251
Nardini, E., Reeves, J. N., Gofford, J., et al. 2015, Science, 347, 860
Nardini, E., Lusso, E., & Bisogni, S. 2019, MNRAS, 482, L134
Ostriker, J. P., Choi, E., Ciotti, L., Novak, G. S., & Proga, D. 2010, ApJ, 722, 642
Parker, M. L., Pinto, C., Fabian, A. C., et al. 2017, Nature, 543, 83
Parker, M. L., Matzeu, G. A., Guainazzi, M., et al. 2018, MNRAS, 480, 2365
Parker, M. L., Longinotti, A. L., Schartel, N., et al. 2019, MNRAS, 490, 683
Parker, M. L., Alston, W. N., Igo, Z., & Fabian, A. C. 2020, MNRAS, 492, 1363
Perna, M., Lanzuisi, G., Brusa, M., Mignoli, M., & Cresci, G. 2017, A&A, 603, A99
Petrucci, P. O., Paltani, S., Malzac, J., et al. 2013, A&A, 549, A73
Petrucci, P.-O., Ursini, F., De Rosa, A., et al. 2018, A&A, 611, A59
Piconcelli, E., Jimenez-Bailón, E., Guainazzi, M., et al. 2004, MNRAS, 351, 161
Piconcelli, E., Jimenez-Bailón, E., Guainazzi, M., et al. 2005, A&A, 432, 15
Pinto, C., Alston, W., Parker, M. L., et al. 2018, MNRAS, 476, 1021
Porquet, D., Kaastra, J. S., Page, K. L., et al. 2004a, A&A, 413, 913
Porquet, D., Reeves, J. N., Uttley, P., & Turner, T. J. 2004b, A&A, 427, 101

Porquet, D., Reeves, J. N., Grosso, N., Braito, V., & Lobban, A. 2021, A&A, 654, A89
Pounds, K. A., & Reeves, J. N. 2009, MNRAS, 397, 249
Proga, D., Stone, J. M., & Kallman, T. R. 2000, ApJ, 543, 686
Protassov, R., van Dyk, D. A., Connors, A., Kashyap, V. L., & Siemiginowska, A. 2002, ApJ, 571, 545
Reeves, J. N., & Braito, V. 2019, ApJ, 884, 80
Reeves, J. N., O'Brien, P. T., & Ward, M. J. 2003, ApJ, 593, L65
Reeves, J. N., Porquet, D., Braito, V., et al. 2013, ApJ, 776, 99
Reeves, J. N., Braito, V., Nardini, E., et al. 2016, ApJ, 824, 20
Reeves, J. N., Braito, V., Nardini, E., et al. 2018a, ApJ, 854, L8
Reeves, J. N., Lobban, A., & Pounds, K. A. 2018b, ApJ, 854, 28
Reeves, J. N., Braito, V., Chartas, G., et al. 2020, ApJ, 895, 37
Reynolds, C. S. 1997, MNRAS, 286, 513
Richards, G. T., Kruczek, N. E., Gallagher, S. C., et al. 2011, AJ, 141, 167
Ross, R. R., & Fabian, A. C. 2005, MNRAS, 358, 211
Różańska, A., Malzac, J., Belmont, R., Czerny, B., & Petrucci, P. O. 2015, A&A, 580, A77
Saez, C., & Chartas, G. 2011, ApJ, 737, 91
Sako, M., Kahn, S. M., Paerels, F., & Liedahl, D. A. 2000, ApJ, 543, L115
Salpeter, E. E. 1964, ApJ, 140, 796
Schmidt, M., & Green, R. F. 1983, ApJ, 269, 352
Serafinelli, R., Tombesi, F., Vagnetti, F., et al. 2019, A&A, 627, A121
Sim, S. A., Long, K. S., Miller, L., & Turner, T. J. 2008, MNRAS, 388, 611
Sim, S. A., Miller, L., Long, K. S., Turner, T. J., & Reeves, J. N. 2010, MNRAS, 404, 1369
Sirressi, M., Cicone, C., Severgnini, P., et al. 2019, MNRAS, 489, 1927
Sądowski, A., & Gaspari, M. 2017, MNRAS, 468, 1398
Smith, R. K., Brickhouse, N. S., Liedahl, D. A., & Raymond, J. C. 2001, ApJ, 556, L91
Steenbrugge, K. C., Kaastra, J. S., de Vries, C. P., & Edelson, R. 2003, A&A, 402, 477
Steenbrugge, K. C., Kaastra, J. S., Crenshaw, D. M., et al. 2005, A&A, 434, 569
Strüder, L., Briel, U., Dennerl, K., et al. 2001, A&A, 365, L18
Tashiro, M., Maejima, H., Toda, K., et al. 2020, SPIE Conf. Ser., 11444, 1144422
Temi, P., Gaspari, M., Brighenti, F., et al. 2022, ApJ, 928, 150
Tombesi, F., Cappi, M., Reeves, J. N., et al. 2010, A&A, 521, A57
Tombesi, F., Cappi, M., Reeves, J. N., et al. 2011, ApJ, 742, 44
Tombesi, F., Cappi, M., Reeves, J. N., & Braito, V. 2012, MNRAS, 422, L1
Tombesi, F., Cappi, M., Reeves, J. N., et al. 2013, MNRAS, 430, 1102
Tombesi, F., Meléndez, M., Veilleux, S., et al. 2015, Nature, 519, 436
Torrey, P., Hopkins, P. F., Faucher-Giguère, C.-A., et al. 2020, MNRAS, 497, 5292
Tozzi, G., Cresci, G., Marasco, A., et al. 2021, A&A, 648, A99
Turner, M. J. L., Abbey, A., Arnaud, M., et al. 2001, A&A, 365, L27
Ursini, F., Petrucci, P. O., Bianchi, S., et al. 2020, A&A, 634, A92
Vaughan, S., Edelson, R., Warwick, R. S., & Uttley, P. 2003, MNRAS, 345, 1271
Vietri, G., Misawa, T., Piconcelli, E., et al. 2022, A&A, 668, A87
Vignali, C., Iwasawa, K., Comastri, A., et al. 2015, A&A, 583, A141
Walton, D. J., Nardini, E., Fabian, A. C., Gallo, L. C., & Reis, R. C. 2013, MNRAS, 428, 2901
Waters, T., Proga, D., & Dannen, R. 2021, ApJ, 914, 62
Wilkes, B. J., & Elvis, M. 1987, ApJ, 323, 243
Wilkins, D. R., & Fabian, A. C. 2012, MNRAS, 424, 1284
Wilms, J., Allen, A., & McCray, R. 2000, ApJ, 542, 914
Wittor, D., & Gaspari, M. 2020, MNRAS, 498, 4983
Woods, D. T., Klein, R. I., Castor, J. I., McKee, C. F., & Bell, J. B. 1996, ApJ, 461, 767
Xie, Y., Li, A., & Hao, L. 2017, ApJS, 228, 6
Xu, Y., García, J. A., Walton, D. J., et al. 2021, ApJ, 913, 13
Yang, H. Y. K., Gaspari, M., & Marlow, C. 2019, ApJ, 871, 6
Zanchettin, M. V., Feruglio, C., Bischetti, M., et al. 2021, A&A, 655, A25
Zubovas, K., & King, A. 2012, ApJ, 745, L34
Zubovas, K., & King, A. 2016, MNRAS, 462, 4055
Zubovas, K., & Nardini, E. 2020, MNRAS, 498, 3633

1   Department of Physics and Astronomy (DIFA), University of Bologna, Via Gobetti, 93/2, 40129 Bologna, Italy
    e-mail: gabriele.matzeu@unibo.it
2   INAF – Osservatorio di Astrofisica e Scienza dello Spazio di Bologna, Via Gobetti, 93/3, 40129 Bologna, Italy
3   European Space Agency (ESA), European Space Astronomy Centre (ESAC), 28691 Villanueva de la Cañada, Madrid, Spain
4   Dipartimento di Matematica e Fisica, Universitá degli Studi Roma Tre, Via della Vasca Navale 84, 00146 Roma, Italy

[5] Space Telescope Science Institute, 3700 San Martin Drive, Baltimore, MD 21218, USA

[6] INAF – Osservatorio Astrofisico di Arcetri, Largo Enrico Fermi 5, 50125 Firenze, Italy

[7] Department of Physics and Astronomy, College of Charleston, Charleston, SC 29424, USA

[8] Space Science Data Center – ASI, Via del Politecnico s.n.c., 00133 Roma, Italy

[9] INAF – Osservatorio Astronomico di Roma, Via Frascati 33, 00078 Monte Porzio Catone (Roma), Italy

[10] Univ. Grenoble Alpes, CNRS, IPAG, 621 Av. Centrale, 38400 Saint-Martin-d'Hères, France

[11] Instituto de Astronomía, Universidad Nacional Autónoma de México, Circuito Exterior, Ciudad Universitaria, Ciudad de México 04510, México

[12] Department of Physics, University of Rome 'Tor Vergata', Via della Ricerca Scientifica 1, 00133 Rome, Italy

[13] Department of Astronomy, University of Maryland, College Park, MD 20742, USA

[14] NASA/Goddard Space Flight Center, Code 662, Greenbelt, MD 20771, USA

[15] INAF – Istituto di Astrofisica e Planetologia Spaziali, Via Fosso del Cavaliere, 00133 Roma, Italy

[16] Centro de Astrobiología (CSIC-INTA), Camino Bajo del Castillo s/n, Villanueva de la Cañada, 28692 Madrid, Spain

[17] Department of Astrophysical Sciences, Princeton University, 4 Ivy Lane, Princeton, NJ 08544-1001, USA

[18] Physics Department, The Technion, 32000 Haifa, Israel

[19] INAF – Osservatorio Astronomico di Trieste, Via G. B. Tiepolo 11, 34143 Trieste, Italy

[20] Department of Astronomy, The Ohio State University, 140 West 18th Avenue, Columbus, OH 43210, USA

[21] Center for Cosmology and Astroparticle Physics, 191 West Woodruff Avenue, Columbus, OH 43210, USA

[22] SRON Netherlands Institute for Space Research, Niels Bohrweg 4, 2333 CA Leiden, The Netherlands

[23] Departament de Física, EEBE, Universitat Politècnica de Catalunya, Av. Eduard Maristany 16, 08019 Barcelona, Spain

[24] ESA – European Space Research and Technology Centre (ESTEC), Keplerlaan 1, 2201 AZ Noordwijk, The Netherlands

[25] Leiden Observatory, PO Box 9513, 2300 RA Leiden, The Netherlands

[26] Department of Physics, Institute for Astrophysics and Computational Sciences, The Catholic University of America, Washington, DC 20064, USA

[27] Dipartimento di Fisica e Astronomia, Università di Firenze, via G. Sansone 1, 50019 Sesto Fiorentino, Firenze, Italy

[28] INAF – Osservatorio Astronomico di Brera, Via Bianchi 46, 23807 Merate (LC), Italy

[29] Department of Physics & Astronomy, University of Nevada, Las Vegas, USA

[30] Department of Physics & Astronomy, University of Leicester, Leicester LE1 7RH, UK

[31] Kavli Institute for Cosmology, University of Cambridge, Madingley Road, Cambridge CB3 0HA, UK

[32] Cavendish Laboratory, University of Cambridge, 19 J. J. Thomson Avenue, Cambridge CB3 0HE, UK

[33] Max-Planck-Institut für extraterrestrische Physik, Giessenbachstraße 1, 85748 Garching bei München, Germany

Appendix A: Signal to noise optimisation method

By following the Piconcelli et al. (2004) optimisation method, we maximised the level of background that can be tolerated resulting into an increase of the S/N. This is carried out by testing, through an iterative process, different extraction source radii and for each radius the level of the background, defined as max background, is derived together with the corresponding S/N.

For observations that are not affected by background flares, the background level remains stable along the exposure and, consequently, there is no need to filter-out any particular time intervals. In this case the max background level is stable and independent from the extraction region radius, and the highest S/N is achieved at the maximum allowed extraction radius, which, in our case, is $r = 40$ arcsec. Differently, for observations affected by strong background flares, the dimension of the extraction regions regulates the dominance of the source signal over the background and thus, the max background level changes as a function of the extraction radius itself. For those cases, the S/N depends on the interplay between the relative source dominance – which tends to diminish as the source extraction radius increases, leading to a lower acceptable max background – and the overall source counts, which tend to increase as the extraction radius increases. This interplay, at the end, defines a couple of values for the extraction radius and the max background for which we have the maximum S/N for our data. Between the extreme cases, we have observations for which there are short and/or weak background flares. In these cases we can appreciate some changes of the max background, but the best extraction region has the dimensions of the maximum allowed radius. It is finally worth noting how the different effective areas among MOS and pn drive different instrument responses to background flares and, thus, different S/N and max background curves.

Appendix B: Summary of SUBWAYS observations

In Table B.1 we summarise the individual observation details from the 22 SUBWAYS targets such as their ID, net exposure time and the corresponding total number of counts for each EPIC detector. We also tabulated the maximum S/N obtained from our optimisation procedure. We discarded all the observations with a total count $\lesssim 1500$ in the EPIC-pn.

Table B.1. Optimised EPIC data reduction: 4–10 keV band

Source[1]	XMM ObsID	Date[2]	Net Exposure[3] (ksec)			maxS/N[4]			Total counts[5]		
		yyyy-mm-dd	pn	MOS 1	MOS 2	pn	MOS 1	MOS 2	pn	MOS 1	MOS 2
SUBWAYS targets observed during AO18 cycle											
PG0052+251	0841480101	2019-07-15	34.4	50.1	50.1	92.3	236.2	238.9	9119	3771	4229
PG0953+414	0841480201	2020-04-14	45.5	50.9	50.9	69.2	208.8	204.9	5244	1869	1897
PG1626+554	0841480401	2019-05-27	51.4	60.9	60.9	72.2	205.4	206.4	5902	2300	2375
PG1202+281	0841480501	2020-06-29	46.8	54.9	57.6	78.6	179.1	181.8	7141	2671	2746
PG1435−067	0841480601	2019-07-24	42.3	59.4	64.3	39.8	108.4	112.7	2022	899	973
SDSS J144414+0633	0841480701	2019-07-28	66.3	80.0	82.7	78.1	188.1	193.9	7067	2480	2774
2MASS J165315+2349	0841480801	2020-02-11	59.8	78.0	78.6	82.3	57.9	63.1	7652	2641	3039
PG1216+069	0841480901	2020-06-05	63.4	78.6	81.2	65.2	164.7	167.9	4792	1807	1902
PG0947+396	0841481001 (Obs 1)	2019-11-25	31.1	43.9	44.8	32.9	100.8	105.9	1682	789	847
	0841482301 (Obs 2)	2020-04-17	45.7	54.1	54.1	45.6	119.3	117.5	2436	908	947
WISE J053756−0245	0841481101	2020-03-02	69.8	90.3	91.4	57.6	112.4	113.7	3900	1563	1576
HB 891529+050	0841481301	2019-08-22	75.3	92.9	93.0	56.3	134.1	134.6	3592	1407	1439
PG1307+085	0841481401	2020-01-22	73.1	86.9	86.8				10547	3971	3787
PG1425+267	0841481501	2020-02-05	73.3	89.9	90.2	63.7	152.2	152.0	4708	2013	2004
PG1352+183	0841481601	2020-01-26	74.4	93.1	93.0	58.3	173.6	171.8	3951	1646	1685
2MASS J105144+3539	0841481701	2020-05-26	80.3	95.3	93.0	41.6	59.1	60.5	2139	811	859
2MASS J0220−0728	0841481901	2020-02-03	77.1	101.9	102.2	57.5	128.1	130.8	3856	1661	1678
LBQS 1338−0038	0841482101	2020-02-01	91.6	114.3	114.4	81.9	202.9	201.3	7775	3085	3139
SUBWAYS targets observed prior AO18 cycle											
PG0804+761	0102040401	2000-11-04	2.33	6.56	6.56		138.9	141.0	1823	845	889
	0605110101	2010-03-10	29.2	27.6	27.6	78.3	270.2	270.1	8426	3070	3316
	0605110201	2010-03-12	25.2	35.1	35.1	67.1	270.2	238.0	5741	3006	2547
PG1416−129	0203770201	2004-07-14	44.3	48.9	49.0	68.9	133.8	134.5	5693	1997	2037
PG1402+261	0400200101	2006-12-21	28.0	16.6	16.6	39.7			1752	674	683
	0830470101	2018-12-17	67.2	75.5	75.5	59.7	201.0	197.8	3894	1347	1531
HB89 1257+286	0204040101	2004-06-06	72.8	85.3	85.4	70.3	185.2	186.6	5374	2125	2011
	0204040201	2004-06-18	79.1	91.9	93.6	57.7	166.2	166.6	3880	1690	1613
	0204040301	2004-07-12	77.4	96.3	96.4	60.5	162.4	163.5	4341	1750	1856
	0304320201	2005-06-27	64.1	76.7	78.6	61.4	152.7	155.8	4211	1605	1551
	0304320301	2005-06-28	46.2	54.1	54.3	45.3	119.5	123.1	2498	953	1001
	0304320801	2006-06-06	47.5	62.3	62.5	54.0	154.1	154.0	3539	1441	1546
PG1114+445	0109080801	2002-05-14	37.0	42.2	42.2	59.2	93.4	92.4	3787	1351	1293
	0651330101	2010-05-19	24.5	29.4	30.0	41.9	54.9	55.4	1922	682	778
	0651330301	2010-05-23	30.3	34.3	34.3	32.2	50.2	51.2	1802	626	627
	0651330401	2010-06-10	29.9	38.0	38.5	36.2	63.7	65.5	1861	853	937
	0651330501	2010-06-14	25.4	29.8	29.6	33.1	55.3	55.1	1843	710	715
	0651330601	2010-11-08	18.5	30.1	30.1	51.6	82.6	83.4	2838	1289	1248
	0651330701	2010-11-16	19.5	26.1	26.1	43.6	68.6	68.6	2137	915	937
	0651330801	2010-11-18	23.6	28.4	29.6	43.9	63.8	63.7	2053	794	857
	0651330901	2010-11-20	22.9	26.9	27.5	45.6	69.3	69.0	2261	906	1000
	0651331001	2010-11-26	21.4	25.1	25.0	41.0	59.9	59.7	1914	658	739
	0651331101	2010-12-12	17.1	6.89	6.72	38.7			1672	553	638

Notes. (1) Source name; (2) Starting date of observation; (3) Net exposure after background optimisation; (4) EPIC optimum S/N in the 4–10 keV (pn) and 0.3–10 keV (MOS) band and it is not reported in coadded spectra; (5) EPIC total net count in the 4–10 keV band.

Appendix C: Spectral binning

In this analysis we we were interested in searching narrow and strong absorption features in the EPIC spectra. After maximising the S/N, an additional and crucial step was to carefully include the appropriate choice of an optimal spectral binning in order to avoid the loss of information in the search of weak features like UFOs. We applied the four spectral binning methods most used in the literature (listed below) and subsequently cross-checked their results: `grpmin1` - We over-sampled the EPIC-pn and EPIC-MOS resolution by imposing that each energy channel contains a minimum of 1 count through the SPECGROUP task within SAS (statistics: Cstat). This resulted in a binning resolution of $\Delta E = 5\,\mathrm{eV}$ and $15\,\mathrm{eV}$ per energy bin throughout the 0.3–10 keV energy band for pn and MOS, respectively, for all the observations. `SN5` - The data were binned to ensure a significance of at least 5σ per energy channel with SPECGROUP (statistics: χ^2). For the pn, such binning resulted in a binning resolution of $\Delta E = 5\,\mathrm{eV}$ at 1 keV and $\Delta E \sim 20\,\mathrm{eV}$ at 6.4 keV, whilst $\Delta E = 15\,\mathrm{eV}$ and $\Delta E \sim 60\,\mathrm{eV}$ for MOS. `OS3grp20` - This binning (also obtained with SPECGROUP) is commonly adopted in the literature and corresponds to an oversampling approximately 3× of the instrumental full width half maximum. Additionally, the data are grouped to a minimum of 20 counts per bin in order to use χ^2 statistics. This binning prescription is a safe approach especially in cases where the level of significance of the measured signal is not known a priory. Such binning yielded a resolution of $\Delta E \sim 40\,\mathrm{eV}$, $\sim 45\,\mathrm{eV}$ at 1 keV and $\Delta E \sim 75\,\mathrm{eV}$, $80\,\mathrm{eV}$ at 6.4 keV in EPIC-pn and -MOS, respectively. *Kaastra–Bleeker* ($\mathcal{KB}$) – The Kaastra & Bleeker (2016) optimal binning option in FTGROUPPHA task within the HEASOFT package (statistics: Cstat) in order to maximise the signal in the spectra. In this sophisticated method, a variable binning scheme is followed so that each bin resolution matches the CCD full width half maximum energy resolution of the EPIC detectors (or at least is not smaller than 1/3). Depending on the spectra in question, the $\mathcal{KB}$ binning produced a EPIC-pn data resolution ranging between $\Delta E \sim 50$–$70\,\mathrm{eV}$ and $\Delta E \sim 100$–$150\,\mathrm{eV}$ at 1 keV and 6.4 keV and a EPIC-MOS resolution between $\Delta E \sim 40$–$60\,\mathrm{eV}$ and $\Delta E \sim 100$–$140\,\mathrm{eV}$ at 1 and 6.4 keV.

Appendix D: Broadband continuum modelling

In this work, despite being mainly focused on the iron K band, we carefully modelled the $0.3 - 10\,\mathrm{keV}$ continuum with the simplest phenomenological solution (see Equation 1). The summary of the best-fitting continuum parameters and the overall statistics, including for each EPIC detector, are tabulated in Table D.1. In Figure D.1 we show the individual plots for each SUBWAYS observation as per in Figure 3. It is important to note that the final errors for the best-fit continuum models are recalculated and propagated to the final continuum plus iron K emission/absorption lines model.

Table D.1. Summary of the phenomenological final best-fitting continuum model parameters of each observation of the SUBWAYS sample

Source	XMM ObsID	Baseline Model: Continuum parameters										Stats				Cross-cal.	
		power–law			bbody$_{low}$		bbody$_{high}$		XABS							MOS 1	MOS 2
		Γ	norm 10^{-3}	$F_{4-10\,keV,obs}$ 10^{-12}	kT_{low} eV	norm$_{low}$ 10^{-5}	kT_{high} eV	norm$_{high}$ 10^{-5}	N_H 10^{21} cm^{-2}	$\log(\xi)$ erg cm s^{-1}	f_{cov} %	C_{pn}/ζ	C_{mos1}/ζ	C_{mos2}/ζ	C_{tot}/ν		
PG0052+251	0841480101	$1.76^{+0.03}_{-0.03}$	$1.71^{+0.48}_{-0.49}$	$4.10^{+0.06}_{-0.06}$	110^{+4}_{-4}	$9.0^{+4.3}_{-2.4}$	248^{+4}_{-4}	$3.2^{+0.8}_{-0.7}$	$6.0^{+1.4}_{-3.4}$	$-1.1^{+0.5}_{-0.4}$	45^{+17}_{-16}	125.7/102	124.4/119	127.0/127	377.1/335	$1.02^{+0.01}_{-0.01}$	$1.04^{+0.01}_{-0.01}$
PG0953+414	0841480201	$1.87^{+0.04}_{-0.04}$	$0.90^{+0.05}_{-0.05}$	$1.81^{+0.04}_{-0.04}$	115^{+3}_{-3}	$8.8^{+0.6}_{-0.6}$	280^{+14}_{-14}	$2.0^{+0.2}_{-0.2}$	$0.88^{+0.20}_{-0.20}$	$1.1^{+0.3}_{-0.2}$	100^{f}	109.7/106	109.7/114	152.5/120	371.8/324	$1.06^{+0.01}_{-0.01}$	$1.08^{+0.01}_{-0.01}$
PG1626+554	0841480401	$1.90^{+0.03}_{-0.03}$	$0.96^{+0.04}_{-0.04}$	$1.80^{+0.03}_{-0.03}$	102^{+5}_{-6}	$4.0^{+0.4}_{-0.4}$	225^{+14}_{-14}	$1.6^{+0.2}_{-0.2}$	$0.86^{+0.23}_{-0.22}$	$0.84^{+0.34}_{-0.23}$	100^{f}	79.0/90	125.2/115	115.1/120	320.1/311	$1.01^{+0.01}_{-0.01}$	$1.05^{+0.01}_{-0.01}$
PG1202+281	0841480501	$1.64^{+0.01}_{-0.01}$	$0.80^{+0.06}_{-0.06}$	$2.43^{+0.04}_{-0.04}$	115^{+7}_{-8}	$2.3^{+0.9}_{-0.7}$	265^{+21}_{-20}	$2.3^{+0.9}_{-0.3}$	$7.4^{+11.1}_{-5.1}$	$0.57^{+0.44}_{-0.53}$	28^{+17}_{-13}	92.1/108	112.6/118	127.0/124	331.8/333	$1.07^{+0.01}_{-0.01}$	$1.08^{+0.01}_{-0.01}$
PG1435−067	0841480601	$1.68^{+0.06}_{-0.06}$	$0.30^{+0.03}_{-0.03}$	$0.80^{+0.05}_{-0.05}$	103^{+4}_{-4}	$1.7^{+0.1}_{-0.1}$	283^{+26}_{-28}	$0.36^{+0.08}_{-0.08}$	—	—	—	86.8/83	124.5/104	159.4/112	370.7/287	$1.02^{+0.02}_{-0.02}$	$1.02^{+0.02}_{-0.02}$
SDSS J144414+0633[⊞]	0841480701	$1.72^{+0.03}_{-0.03}$	$0.65^{+0.23}_{-0.22}$	$1.64^{+0.03}_{-0.03}$	103^{+5}_{-5}	$2.3^{+0.1}_{-0.1}$	259^{+15}_{-15}	$0.96^{+0.09}_{-0.10}$	—	—	—	117.3/91	117.4/118	124.2/124	358.9/321	$1.02^{+0.02}_{-0.01}$	$1.02^{+0.01}_{-0.01}$
2MASS J165315+2349[†]	0841480801	$1.65^{+0.09}_{-0.08}$	$1.00^{+0.20}_{-0.20}$	$2.17^{+0.07}_{-0.07}$	—	—	—	—	—	—	—	74.2/82	83.2/100	105.7/107	263.1/273	$1.01^{+0.03}_{-0.03}$	$1.07^{+0.03}_{-0.03}$
PG1216+069	0841480901	$1.74^{+0.01}_{-0.01}$	$0.48^{+0.02}_{-0.02}$	$1.19^{+0.02}_{-0.02}$	117^{+8}_{-7}	$2.6^{+0.3}_{-0.3}$	276^{+21}_{-20}	$0.95^{+0.12}_{-0.12}$	$1.4^{+1.1}_{-0.8}$	$2.0^{+0.3}_{-0.4}$	100^{f}	83.2/89	122.4/114	141.8/121	347.4/311	$1.03^{+0.01}_{-0.01}$	$1.05^{+0.01}_{-0.01}$
PG0947+396 (Obs 1)	0841481001	$1.71^{+0.06}_{-0.07}$	$0.36^{+0.03}_{-0.03}$	$0.93^{+0.03}_{-0.03}$	110^{+9}_{-9}	$1.3^{+0.2}_{-0.2}$	269^{+29}_{-29}	$0.64^{+0.11}_{-0.11}$	—	—	—	96.8/82	102.0/100	108.2/109	307.0/277	$0.99^{+0.02}_{-0.02}$	$1.03^{+0.02}_{-0.02}$
PG0947+396 (Obs 2)	0841482301	$1.73^{+0.05}_{-0.05}$	$0.33^{+0.02}_{-0.02}$	$0.84^{+0.02}_{-0.02}$	108^{+6}_{-6}	$1.5^{+0.1}_{-0.1}$	274^{+22}_{-22}	$0.59^{+0.08}_{-0.08}$	—	—	—	81.1/84	112.5/107	99.7/112	293.2/293	$1.04^{+0.02}_{-0.02}$	$1.04^{+0.02}_{-0.02}$
WISE J053756−0245	0841481101	$1.65^{+0.05}_{-0.06}$	$0.30^{+0.01}_{-0.01}$	$0.91^{+0.02}_{-0.02}$	—	—	228^{+20}_{-20}	$0.17^{+0.04}_{-0.04}$	—	—	—	96.1/86	121.8/109	121.1/114	339.0/301	$1.06^{+0.02}_{-0.02}$	$1.04^{+0.02}_{-0.02}$
HB 891529+050	0841481301	$1.75^{+0.02}_{-0.05}$	$0.31^{+0.02}_{-0.02}$	$0.77^{+0.03}_{-0.03}$	116^{+13}_{-14}	$0.74^{+0.18}_{-0.15}$	275^{+21}_{-20}	$0.42^{+0.07}_{-0.07}$	$0.68^{+0.42}_{-0.45}$	$1.2^{+0.7}_{-0.5}$	100^{f}	84.3/86	112.1/113	129.4/118	325.7/304	$1.04^{+0.01}_{-0.01}$	$1.04^{+0.01}_{-0.01}$
PG1307+085	0841481401	$1.82^{+0.02}_{-0.02}$	$1.10^{+0.04}_{-0.04}$	$2.28^{+0.03}_{-0.03}$	110^{+3}_{-3}	$6.8^{+0.6}_{-0.6}$	260^{+11}_{-11}	$1.8^{+0.1}_{-0.1}$	$0.98^{+0.20}_{-0.20}$	$0.36^{+0.21}_{-0.21}$	100^{f}	114.8/94	116.1/119	186.5/126	399.4/327	$1.05^{+0.01}_{-0.01}$	$1.02^{+0.01}_{-0.01}$
PG1425+267	0841481501	$1.71^{+0.11}_{-0.11}$	$0.42^{+0.05}_{-0.05}$	$1.09^{+0.02}_{-0.02}$	96^{+6}_{-6}	$2.7^{+0.3}_{-0.3}$	321^{+21}_{-20}	$0.60^{+0.9}_{-0.3}$	$7.6^{+2.1}_{-1.8}$	$2.3^{+0.1}_{-0.1}$	100^{f}	97.8/88	102.4/115	107.5/120	307.6/307	$1.03^{+0.01}_{-0.01}$	$1.05^{+0.01}_{-0.01}$
PG1352+183	0841481601	$1.92^{+0.04}_{-0.04}$	$0.45^{+0.05}_{-0.05}$	$0.85^{+0.01}_{-0.01}$	98^{+5}_{-5}	$1.7^{+0.1}_{-0.1}$	244^{+17}_{-17}	$0.55^{+0.08}_{-0.08}$	—	—	—	119.9/88	128.8/115	112.9/119	361.7/311	$1.03^{+0.01}_{-0.01}$	$1.04^{+0.01}_{-0.01}$
2MASS J105144+3539[‡]	0841481701	$1.56^{+0.02}_{-0.02}$	$0.14^{+0.10}_{-0.05}$	$0.46^{+0.01}_{-0.01}$	—	—	197^{+11}_{-11}	$0.21^{+0.04}_{-0.04}$	$21.9^{+0.3}_{-0.5}$	$0.58^{+0.44}_{-0.52}$	29^{+14}_{-13}	94.7/80	87.2/94	122.3/102	304.3/263	$1.10^{+0.04}_{-0.04}$	$1.02^{+0.03}_{-0.03}$
2MASS J0220−0728	0841481901	$1.67^{+0.05}_{-0.06}$	$0.29^{+0.07}_{-0.07}$	$0.83^{+0.01}_{-0.01}$	—	—	282^{+20}_{-20}	$0.71^{+0.09}_{-0.09}$	$0.72^{+0.33}_{-0.32}$	$0.95^{+0.35}_{-0.31}$	100^{f}	79.7/78	149.7/114	117.6/119	347.0/311	$1.03^{+0.02}_{-0.02}$	$1.05^{+0.02}_{-0.02}$
LBQS 1338−0038	0841482101	$1.69^{+0.03}_{-0.03}$	$0.26^{+0.02}_{-0.02}$	$1.34^{+0.03}_{-0.03}$	119^{+7}_{-8}	$1.7^{+0.3}_{-0.2}$	239^{+27}_{-27}	$0.11^{+0.01}_{-0.01}$	—	—	—	101.5/92	128.8/119	100.1/125	330.4/320	$1.02^{+0.01}_{-0.01}$	$1.03^{+0.01}_{-0.01}$
PG0804+761	0102040401	$1.97^{+0.05}_{-0.05}$	$3.93^{+0.28}_{-0.29}$	$6.71^{+0.21}_{-0.24}$	93^{+6}_{-8}	$3.2^{+0.8}_{-0.8}$	—	—	—	—	—	88.9/92	137.6/112	131.1/112	357.6/302	$1.14^{+0.02}_{-0.02}$	$1.16^{+0.02}_{-0.02}$
	0605110101	$1.96^{+0.03}_{-0.03}$	$3.35^{+0.15}_{-0.15}$	$5.67^{+0.07}_{-0.07}$	92^{+2}_{-2}	$2.1^{+0.7}_{-0.7}$	252^{+1}_{-7}	$0.48^{+0.04}_{-0.04}$	—	—	—	116.2/106	153.0/121	131.9/126	401.0/333	$1.07^{+0.01}_{-0.01}$	$1.09^{+0.01}_{-0.01}$
	0605110201	$2.08^{+0.03}_{-0.03}$	$3.03^{+0.11}_{-0.11}$	$4.23^{+0.08}_{-0.08}$	85^{+3}_{-3}	$1.7^{+0.8}_{-0.7}$	200^{+12}_{-12}	$0.41^{+0.04}_{-0.04}$	—	—	—	129.9/103	133.6/124	139.6/120	403.0/30	$1.04^{+0.01}_{-0.01}$	$1.09^{+0.01}_{-0.01}$
PG1416−129[*]	0203770201	$1.74^{+0.02}_{-0.02}$	$0.69^{+0.17}_{-0.18}$	$2.28^{+0.04}_{-0.04}$	153^{+7}_{-8}	$1.0^{+0.3}_{-0.3}$	—	—	$1.20^{+0.05}_{-0.05}$	$0.80^{+0.51}_{-0.27}$	100^{f}	132.5/109	120.5/118	136.5/118	389.6/335	$1.53^{+0.02}_{-0.02}$	$1.06^{+0.02}_{-0.02}$
PG1402+261	0400200101	$2.00^{+0.05}_{-0.06}$	$0.63^{+0.04}_{-0.04}$	$1.00^{+0.03}_{-0.03}$	90^{+5}_{-5}	$4.2^{+0.3}_{-0.3}$	213^{+18}_{-18}	$1.0^{+0.1}_{-0.2}$	—	—	—	94.7/99	90.0/106	117.2/108	301.9/301	$1.04^{+0.02}_{-0.02}$	$1.09^{+0.02}_{-0.02}$
	0830470101	$2.16^{+0.05}_{-0.05}$	$0.79^{+0.04}_{-0.04}$	$0.90^{+0.02}_{-0.02}$	88^{+5}_{-5}	$3.9^{+0.3}_{-0.3}$	217^{+13}_{-13}	$1.1^{+0.1}_{-0.1}$	—	—	—	122/104	136.4/116	107.0/121	365.3/329	$1.03^{+0.01}_{-0.01}$	$1.05^{+0.01}_{-0.01}$

Table D.1. continued.

Source	XMM ObsID	Γ	power-law norm 10^{-3}	$F_{4-10\,\mathrm{keV,obs}}$ 10^{-12}	bbody$_{\mathrm{low}}$ kT_{low} eV	norm$_{\mathrm{low}}$ 10^{-5}	bbody$_{\mathrm{high}}$ kT_{high} eV	norm$_{\mathrm{high}}$ 10^{-5}	N_{H} 10^{21} cm^{-2}	XABS $\log(\xi)$ erg cm s^{-1}	f_{cov} %	C_{pn}/ζ	C_{mos1}/ζ	C_{mos2}/ζ	C_{tot}/ν	Cross-cal. MOS 1	MOS 2
HB89 1257+286	0204040101	$1.83^{+0.02}_{-0.02}$	$0.59^{+0.47}_{-0.17}$	$1.20^{+0.02}_{-0.02}$	102^{+5}_{-5}	$2.1^{+0.5}_{-0.3}$	229^{+18}_{-15}	$0.89^{+0.39}_{-0.20}$	$6.00^{+4.33}_{-3.71}$	$-0.14^{+0.40}_{-0.63}$	35^{+15}_{-6}	117.2/98	121.7/119	137.5/120	376.4/322	$1.03^{+0.01}_{-0.01}$	$1.05^{+0.01}_{-0.01}$
	0204040201	$1.83^{+0.04}_{-0.04}$	$0.41^{+0.02}_{-0.02}$	$0.87^{+0.02}_{-0.02}$	105^{+5}_{-4}	$2.0^{+0.4}_{-0.3}$	243^{+20}_{-18}	$0.56^{+0.08}_{-0.08}$	$1.00^{+4.32}_{-0.35}$	$-0.27^{+0.48}_{-0.45}$	100^f	111.0/96	151.3/117	157.8/117	420.1/318	$1.03^{+0.01}_{-0.01}$	$1.06^{+0.01}_{-0.01}$
	0204040301	$1.87^{+0.08}_{-0.09}$	$0.52^{+0.08}_{-0.08}$	$1.00^{+0.02}_{-0.02}$	100^{+7}_{-7}	$2.0^{+0.9}_{-0.9}$	222^{+24}_{-19}	$1.2^{+1.1}_{-0.7}$	$13.35^{+...}_{-0.70}$	$-0.52^{+0.67}_{-0.45}$	52^{+15}_{-27}	85.4/96	165.7/119	130.7/119	381.8/319	$1.05^{+0.01}_{-0.01}$	$1.05^{+0.01}_{-0.01}$
	0304320201	$1.78^{+0.05}_{-0.09}$	$0.45^{+0.03}_{-0.03}$	$1.05^{+0.02}_{-0.02}$	113^{+6}_{-7}	$1.3^{+0.3}_{-0.3}$	256^{+27}_{-19}	$0.47^{+0.09}_{-0.09}$	$0.88^{+0.29}_{-0.35}$	$0.60^{+0.31}_{-0.45}$	100^f	93.9/94	104.5/115	91.4/116	289.9/312	$1.03^{+0.01}_{-0.01}$	$1.05^{+0.01}_{-0.01}$
	0304320301	$1.75^{+0.06}_{-0.05}$	$0.39^{+0.07}_{-0.03}$	$0.93^{+0.02}_{-0.02}$	105^{+6}_{-7}	$0.96^{+0.11}_{-0.11}$	266^{+24}_{-23}	$0.43^{+0.08}_{-0.09}$	—	—	—	78.7/91	107.4/112	119.9/113	305.1/306	$1.02^{+0.02}_{-0.01}$	$1.05^{+0.02}_{-0.02}$
	0304320801	$1.82^{+0.03}_{-0.05}$	$0.58^{+0.03}_{-0.04}$	$1.25^{+0.03}_{-0.03}$	100^{+5}_{-5}	$0.51^{+0.9}_{-0.3}$	262^{+25}_{-23}	$0.34^{+0.18}_{-0.18}$	—	—	—	101.2/93	100.0/112	110.7/112	311.9/307	$1.03^{+0.01}_{-0.02}$	$1.03^{+0.01}_{-0.01}$
PG1114+445	0109080801	$1.98^{+0.02}_{-0.03}$	$1.09^{+0.02}_{-0.02}$	$1.54^{+0.03}_{-0.03}$	153^{+12}_{-17}	$1.8^{+0.8}_{-0.8}$	—	—	$73.01^{+0.20}_{-0.27}$; $16.69^{+0.04}_{-0.04}$	$3.00^{+0.03}_{-0.07}$; $1.03^{+0.04}_{-0.08}$	100^f	118.7/104	110.5/108	122.0/99	351.1/297	$1.09^{+0.04}_{-0.02}$	$1.04^{+0.04}_{-0.02}$
	0651330101	$1.71^{+0.15}_{-0.12}$	$0.58^{+0.20}_{-0.12}$	$1.30^{+0.04}_{-0.03}$	110^{+11}_{-10}	$2.1^{+1.5}_{-1.1}$	—	—	$91.65^{+50.22}_{-31.72}$; $16.85^{+...}_{-0.66}$	$2.78^{+0.27}_{-0.13}$; $0.70^{+0.18}_{-0.11}$	100^f	88.0/95	92.8/97	107.5/101	288.3/278	$1.11^{+0.04}_{-0.04}$	$1.11^{+0.04}_{-0.04}$
	0651330301	$1.84^{+0.39}_{-0.11}$	$0.76^{+0.31}_{-0.15}$	$1.23^{+0.06}_{-0.11}$	122^{+13}_{-10}	$3.2^{+1.3}_{-0.1}$	—	—	$124.97^{+...}_{-3.73}$; $27.96^{+...}_{-0.34}$	$3.00^{+0.03}_{-0.03}$; $0.85^{+0.16}_{-0.11}$	100^f	86.0/96	92.2/91	112.2/95	290.3/268	$1.12^{+0.04}_{-0.04}$	$1.07^{+0.04}_{-0.04}$
	0651330401	$1.91^{+0.12}_{-0.14}$	$0.90^{+0.23}_{-0.21}$	$1.42^{+0.07}_{-0.06}$	119^{+14}_{-12}	$2.3^{+1.0}_{-0.1}$	—	—	$79.90^{+5.02}_{-3.08}$; $19.07^{+...}_{-0.32}$	$3.01^{+0.08}_{-0.15}$; $0.87^{+0.15}_{-0.13}$	100^f	113.1/96	103.1/96	106.4/106	323.1/288	$1.09^{+0.03}_{-0.03}$	$1.07^{+0.03}_{-0.03}$
	0651330501	$1.90^{+0.12}_{-0.09}$	$0.97^{+0.25}_{-0.17}$	$1.48^{+0.06}_{-0.11}$	89^{+5}_{-5}	$1.9^{+1.4}_{-0.6}$	—	—	$98.80^{+197.53}_{-33.58}$; $15.81^{+...}_{-0.53}$	$3.00^{+0.22}_{-0.15}$; $-0.17^{+0.20}_{-0.20}$	100^f	95.0/96	115.8/97	127.4/101	338.2/286	$1.07^{+0.04}_{-0.04}$	$1.04^{+0.04}_{-0.04}$
	0651330601	$1.88^{+0.07}_{-0.07}$	$1.38^{+0.45}_{-0.43}$	$2.31^{+0.05}_{-0.09}$	139^{+15}_{-14}	$3.29^{+1.1}_{-1.1}$	—	—	$66.08^{+33.18}_{-28.45}$; $16.70^{+...}_{-0.21}$	$2.95^{+0.08}_{-0.12}$; $0.92^{+0.12}_{-0.11}$	100^f	112.0/98	135.3/106	122.3/109	369.7/300	$1.07^{+0.03}_{-0.03}$	$1.05^{+0.03}_{-0.02}$
	0651330701	$1.90^{+0.10}_{-0.10}$	$1.12^{+0.23}_{-0.20}$	$1.75^{+0.05}_{-0.07}$	112^{+14}_{-13}	$2.6^{+1.1}_{-1.0}$	—	—	$91.24^{+28.70}_{-25.29}$; $16.69^{+...}_{-0.41}$	$2.86^{+0.15}_{-0.11}$; $0.81^{+0.12}_{-0.10}$	100^f	113.0/97	102.9/101	123.3/105	339.4/291	$1.06^{+0.03}_{-0.03}$	$1.06^{+0.03}_{-0.03}$
	0651330801	$1.95^{+0.11}_{-0.11}$	$1.03^{+0.26}_{-0.20}$	$1.47^{+0.04}_{-0.09}$	102^{+14}_{-13}	$1.5^{+1.1}_{-1.0}$	—	—	$119.34^{+43.03}_{-32.14}$; $18.16^{+...}_{-0.53}$	$2.89^{+0.14}_{-0.11}$; $0.89^{+0.17}_{-0.13}$	100^f	85.6/96	83.8/100	134.6/104	304.0/288	$1.04^{+0.03}_{-0.03}$	$1.03^{+0.03}_{-0.03}$
	0651330901	$1.80^{+0.10}_{-0.09}$	$0.88^{+0.19}_{-0.14}$	$1.72^{+0.04}_{-0.08}$	108^{+14}_{-13}	$3.3^{+1.1}_{-1.0}$	—	—	$85.35^{+31.26}_{-27.47}$; $16.77^{+...}_{-0.38}$	$2.93^{+0.09}_{-0.10}$; $0.93^{+0.10}_{-0.13}$	100^f	96.0/96	65.3/101	113.2/105	274.2/290	$1.12^{+0.03}_{-0.03}$	$1.11^{+0.03}_{-0.03}$
	0651331001	$1.75^{+0.10}_{-0.09}$	$0.69^{+0.19}_{-0.14}$	$1.49^{+0.05}_{-0.06}$	106^{+14}_{-13}	$3.3^{+1.1}_{-1.0}$	—	—	$71.07^{+34.65}_{-21.34}$; $16.78^{+...}_{-0.38}$	$2.99^{+0.07}_{-0.12}$; $1.00^{+0.13}_{-0.10}$	100^f	92.4/95	91.1/98	78.7/103	262.2/284	$1.08^{+0.04}_{-0.03}$	$1.07^{+0.04}_{-0.03}$
	0651331101	$1.84^{+0.12}_{-0.10}$	$0.94^{+0.24}_{-0.19}$	$1.60^{+0.05}_{-0.08}$	109^{+13}_{-13}	$2.1^{+1.0}_{-1.0}$	—	—	$92.09^{+36.90}_{-31.35}$; $16.57^{+0.17}_{-0.11}$	$2.90^{+0.12}_{-0.13}$; $0.85^{+0.17}_{-0.13}$	100^f	112.2/94	72.7/98	122.0/102	306.9/282	$0.99^{+0.04}_{-0.03}$	$1.05^{+0.04}_{-0.04}$

Notes. In the best-fit models the iron K emission and absorption lines, with their Gaussians model parameters are included and reported separately in Table 2. The $N\mathcal{H}M$ used in Sect. 4.4 consist of the best-fitting models reported here minus the Gaussian absorption components. All the WA components are required at $P_F > 99\%$. Flux in the 4–10 keV band in units of (erg cm^{-2} s^{-1}). Reduced Cstat and number of degrees of freedom (ν) corresponding to the final best-fit model. $C-$stat using the number of bins (ξ) in each EPIC detector and the total $C-$stat with the degree of freedoms (ν) corresponding to the final best-fit model. † A narrow (10eV) Gaussian absorption line of rest-frame energy of $E = 3.51 \pm 0.06$ keV was required at 3σ (99.7%) confidence level. ‡ Seyfert 2 target with an intrinsic neutral absorber with column density of $\log(N_{\mathrm{H}}/\mathrm{cm}^{-2}) = 23.25^{+0.02}_{-0.02}$. The soft X-ray band < 2 keV was modelled with two thermal emission components with apec yielding $kT_{\mathrm{low}} = 145^{+34}_{-36}$ eV, norm$_{\mathrm{low}} = 1.7^{+2.3}_{-0.5} \times 10^{-5}$ and $kT_{\mathrm{high}} = 732^{+21}_{-20}$ eV, norm$_{\mathrm{low}} = 2.3^{+0.9}_{-0.3} \times 10^{-6}$ with normalisations in unit of $\frac{10^{-14}}{4\pi[D_A(1+z)]^2} \int n_e n_{\mathrm{H}} dV$ where D_A is the angular diameter distance to the source in cm, n_e and n_{H} are the electron and H densities (cm^{-3}), respectively. A narrow/strong Gaussian emission line of $E = 2.35 \pm 0.04$ keV was required at 3.6σ ($>99.9\%$) confidence level. ‡ Intrinsic neutral absorber with $\log(N_{\mathrm{H}}/\mathrm{cm}^{-2}) = 21.83^{+0.01}_{-0.01}$ required at $P_F > 99.99\%$ and two narrow soft X-ray emission at $E_{\mathrm{rest}} = 0.54^{+0.03}_{-0.03}$ keV and $E_{\mathrm{rest}} = 0.75^{+0.02}_{-0.03}$ keV both at $P_F > 99.99\%$.
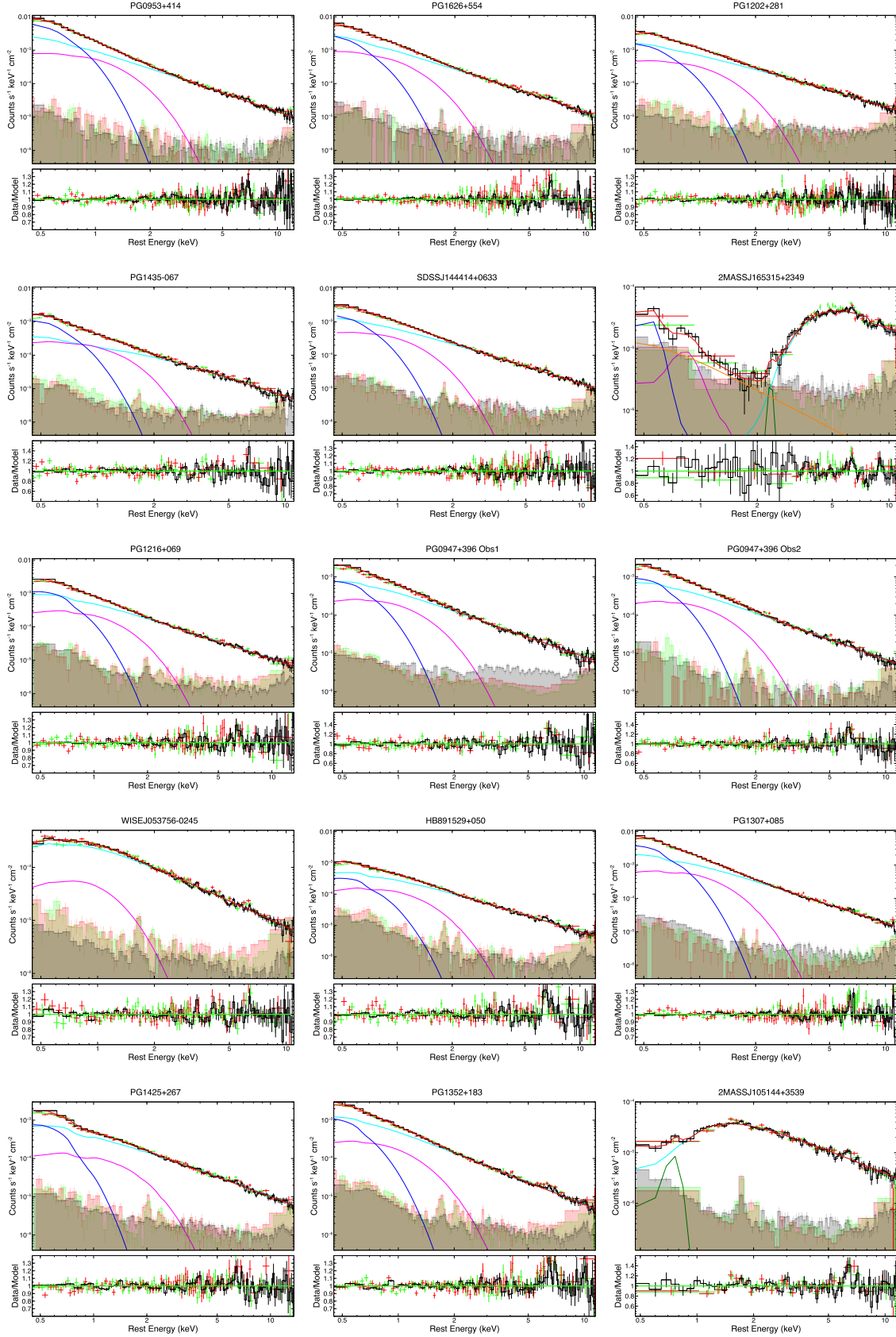
Fig. D.1. Broadband fitting and Fe K residuals of the *XMM-Newton* observations in the SUBWAYS sample. The EPIC-pn (black), MOS 1 (red), and MOS 2 (green) spectra, the corresponding background spectra (shaded area), and the best-fit model (solid red) are plotted. The individual model components are: absorbed power-law (cyan), black-body low- *kT* (blue) and high-*kT* (magenta), soft X-ray Gaussian line (dark green), and scattered power-law (orange). EPIC-MOS are visually binned to 10σ for clarity.
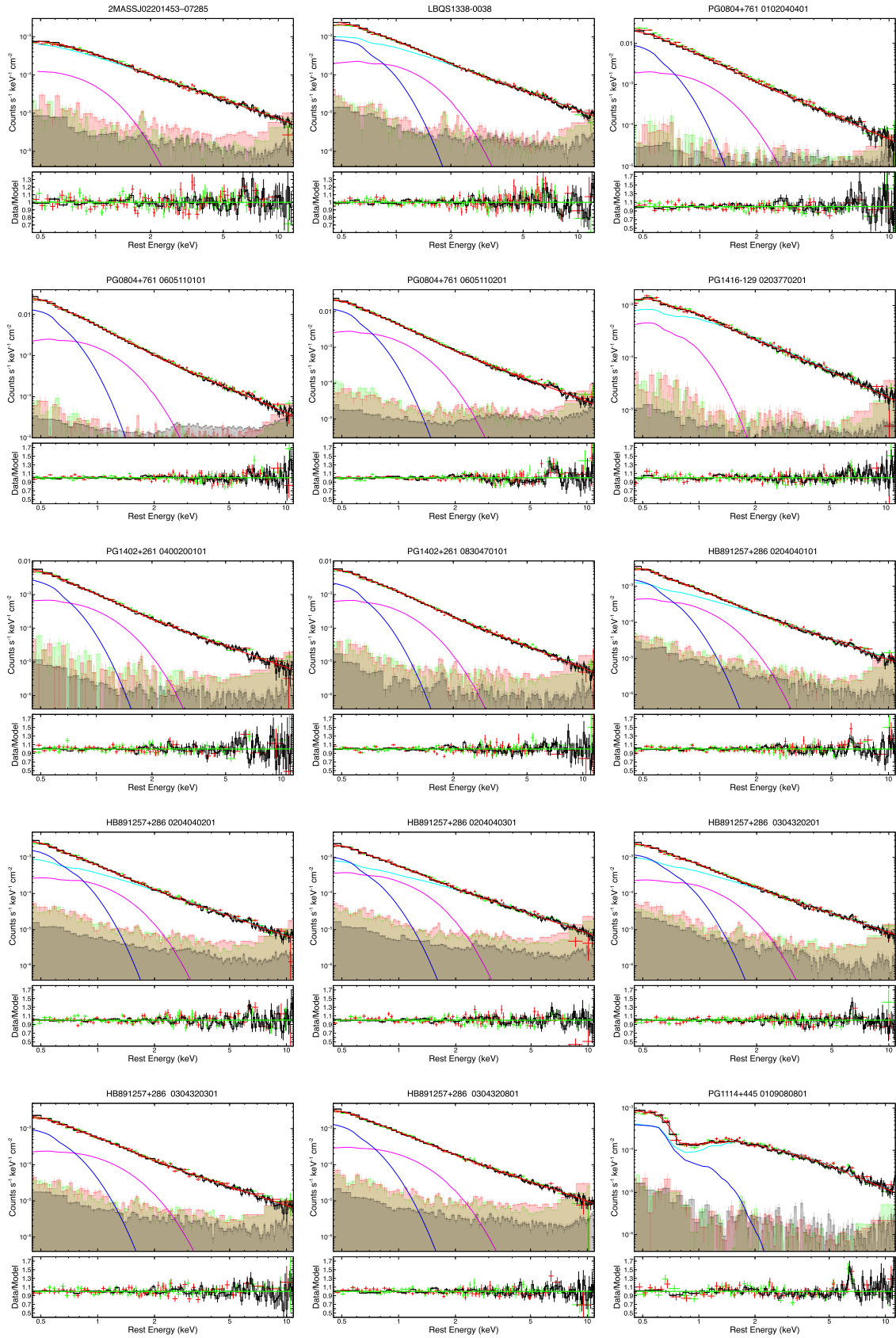
Fig. D.1. continued.
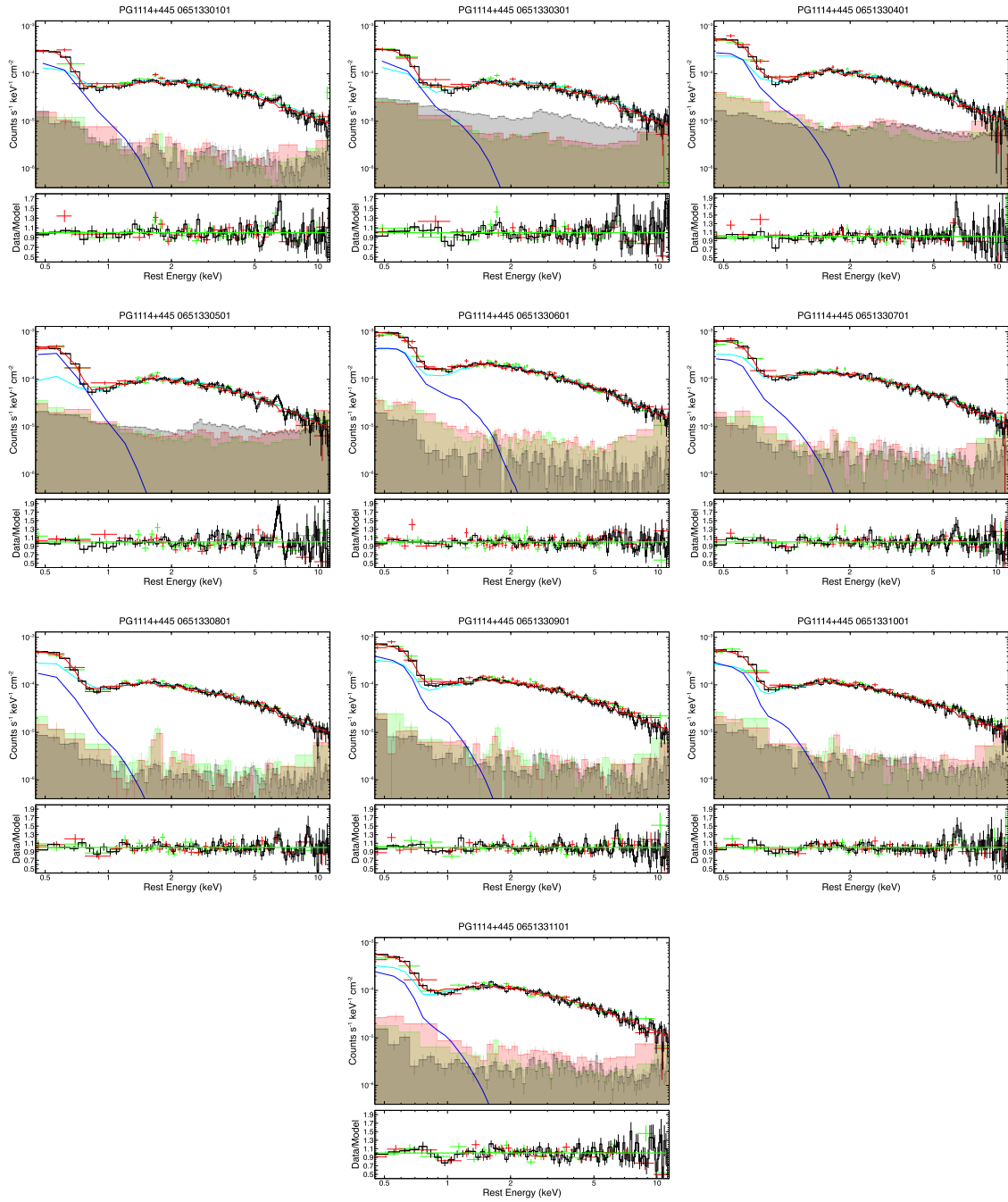
Fig. D.1. continued.

Appendix E: Blind-line search results

As in Figure 4, we shown the residual (top) and blind-scan search contours (bottom) for the remaining 39 in Appendix E.1.
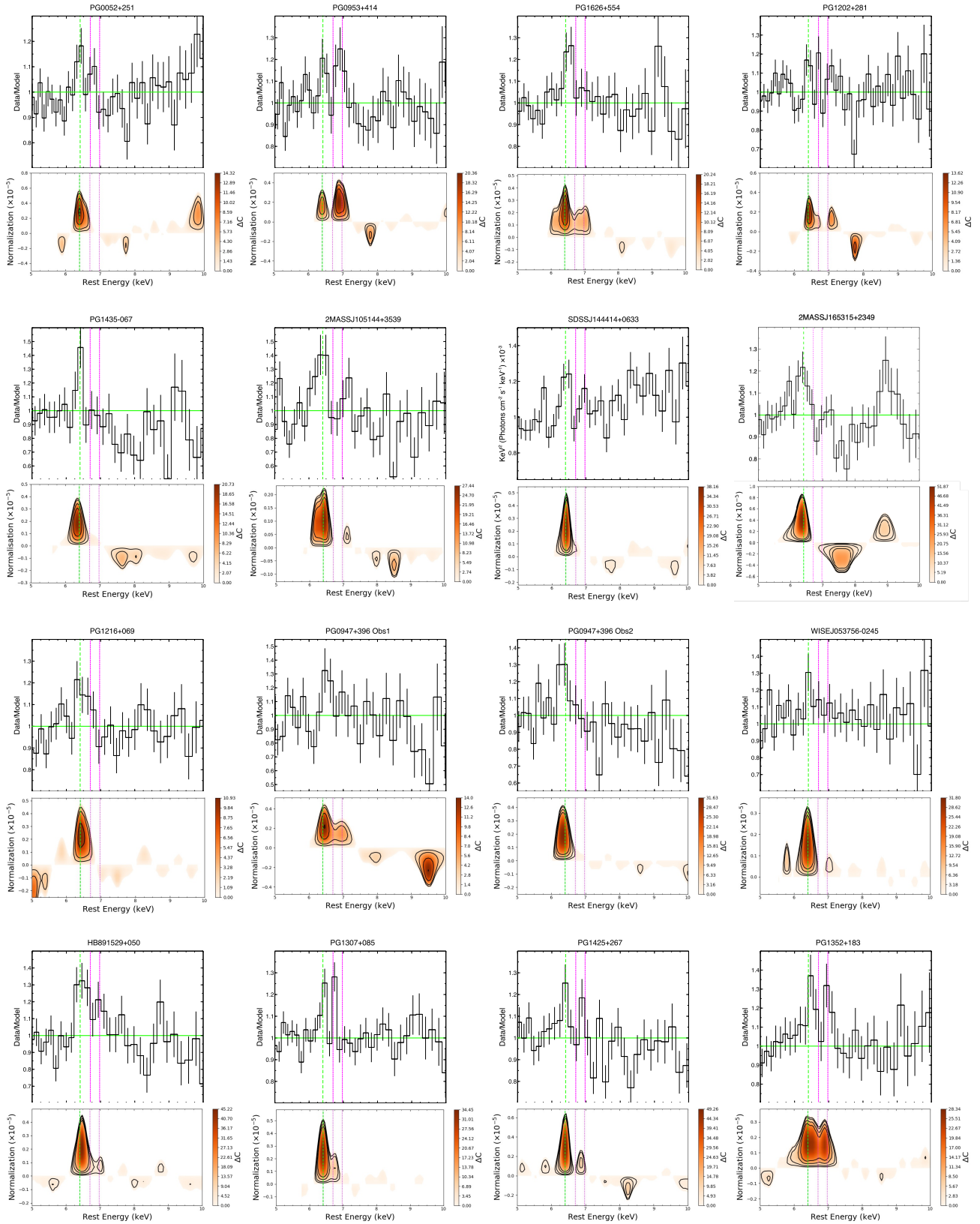

Fig. E.1. Blind line search results, as in Figure 4, for the SUBWAYS sample with the corresponding residuals of the EPIC-pn spectrum in the rest-frame energy between 5 and 10 keV.
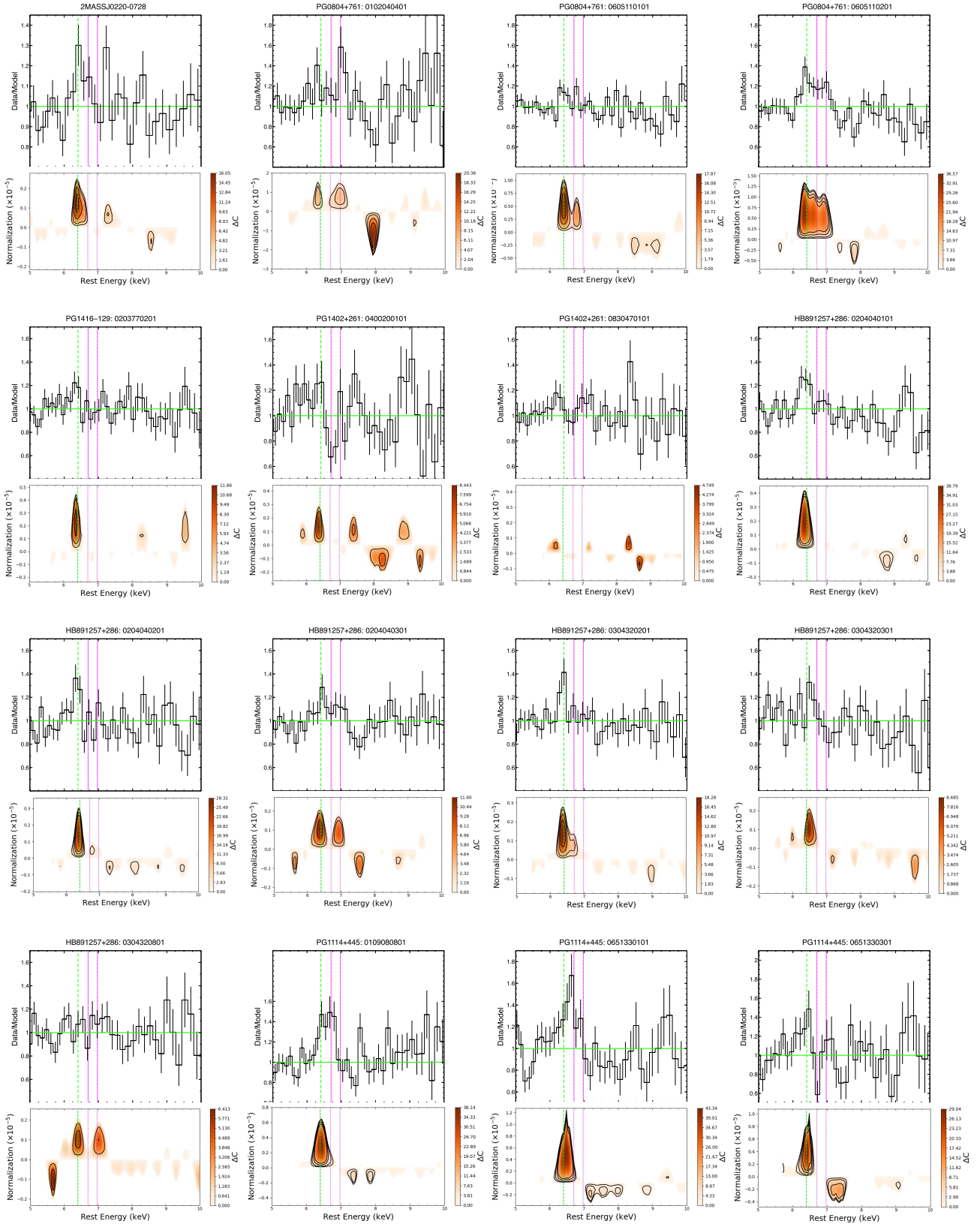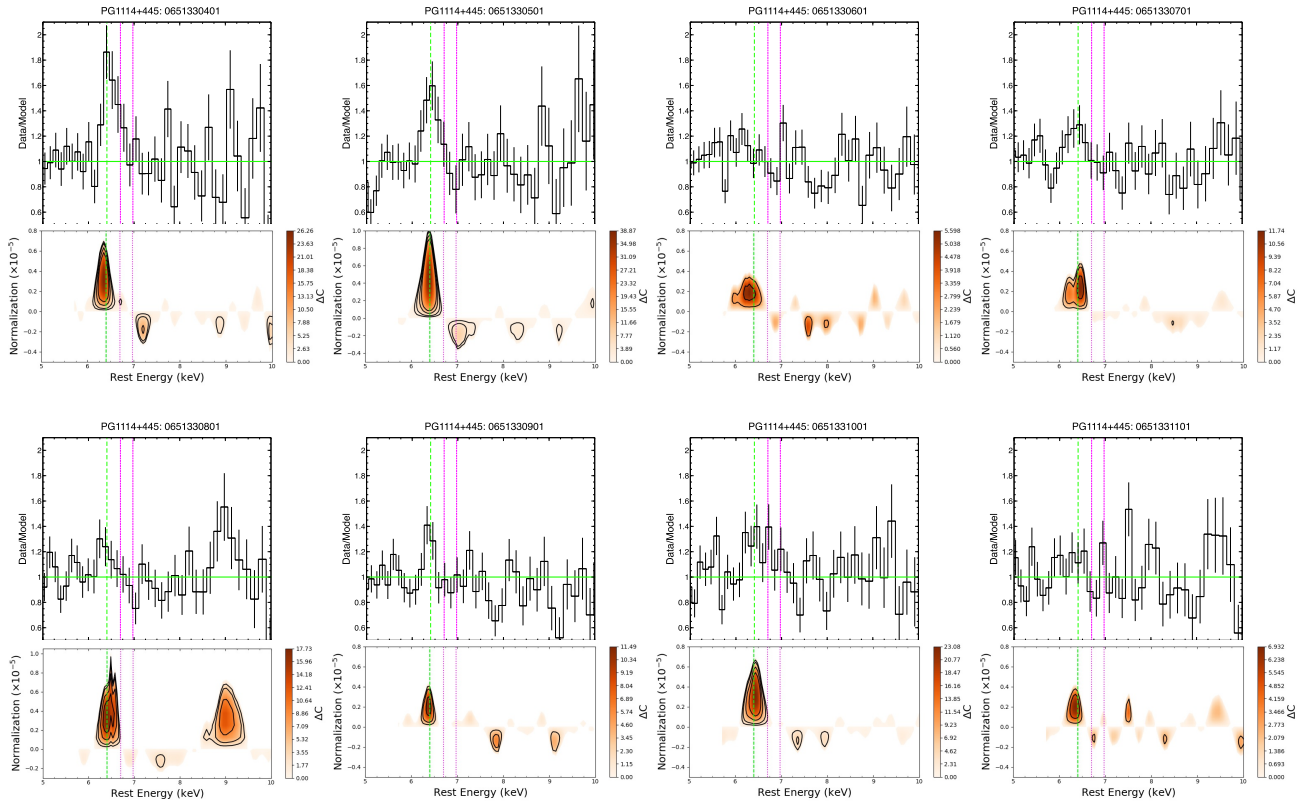
Fig. E.1. continued.

Fig. E.1. continued.